buildings

MDPI

Article

Experimental Investigation and Embodied Carbon Assessment of Self-Compacting Concrete with Granite Powder and Ground Granulated Blast-Furnace Slag

Abdullah Alshahrani [1,2], Haidar Al Haydar [1], Turki Al Alharith [1], Muhannad Al Haidan [1], Ayman Almutlaqah [1,2], Abdulaziz Aldawish [3,4,*], Mohammed Abu Saq [1] and Abdulrahman Almajadiah [5]

[1] Department of Civil Engineering, College of Engineering, Najran University, Najran 61441, Saudi Arabia; aalshahranie@nu.edu.sa (A.A.); yamd4242@gmail.com (T.A.A.); mohnad32x@gmail.com (M.A.H.); aaalmutlaqa@nu.edu.sa (A.A.); miabusaq@nu.edu.sa (M.A.S.)
[2] Science and Engineering Research Center, Najran University, Najran 61441, Saudi Arabia
[3] School of Engineering, Cardiff University, Cardiff CF24 3AA, UK
[4] College of Engineering and Energy, Abdullah Al Salem University, Khaldiya 72303, Kuwait
[5] Architectural Engineering Department, College of Engineering, Najran University, Najran 61441, Saudi Arabia; amalmajadiah@nu.edu.sa
* Correspondence: aldawisha@cardiff.ac.uk

Abstract

Self-compacting concrete (SCC) requires a high powder content, which makes it clinker-intensive. The combined use of a waste mineral powder and a latent hydraulic slag to reduce this clinker content has rarely been examined. This study evaluated waste granite powder (GP) from Najran, Saudi Arabia, combined with ground granulated blast furnace slag (GGBFS) at a 1:2 mass ratio as a cement replacement (0, 15, 30 and 45%) in SCC at a water-to-binder ratio of 0.40. Fresh properties, strength, water penetration, microstructure and embodied carbon were assessed. All mixtures met SCC filling and passing-ability requirements. Cement dilution reduced 7-day strength by up to 60%, but at 28 days the blended mixtures reached 49.8–55.4 MPa (control 56.0 MPa), and at 90 days the 45% mixture reached 83.8 MPa, 9% above the control. Splitting tensile strength increased by up to 20%, water penetration depth decreased by 27.8–61.1% and embodied carbon decreased by up to 30.4%. Strength formation followed two stages: a dilution-controlled stage (strength efficiency per unit cement $K \leq 1.07$ at 7 days) and a reaction-controlled stage in which K reached 1.99 at 90 days. The approach is transferable to other granite-processing and steel-producing regions for low-carbon structural and precast SCC.

Keywords: self-compacting concrete; waste granite powder; ground granulated blast furnace slag; embodied carbon; sustainable construction; structural and precast elements

Check for updates

Academic Editor: Xiaoyong Wang

Received: 29 October 2026
Revised: 16 November 2026
Accepted: 25 November 2026
Published: 29 November 2026

Copyright: © 2026 by the authors. Licensee MDPI, Basel, Switzerland. This article is an open access article distributed under the terms and conditions of the Creative Commons Attribution (CC BY) license.

1. Introduction

Concrete is one of the world's most widely used construction materials, and its enormous scale of production places considerable pressure on natural resources and the environment through the extraction of raw materials, energy-intensive processing, and greenhouse gas emissions. Within the concrete life cycle, Portland cement represents the principal environmental hotspot because clinker production involves both the calcination of limestone and the combustion of fuels, resulting in substantial direct and indirect CO_2 emissions [1]. Cement production alone is estimated to contribute approximately 5–8% of global CO_2 emissions, and the demand for cementitious materials is expected to continue increasing

with population growth, urbanization, infrastructure development, and rapid construction activity in developing regions [2,3]. This growing demand highlights a fundamental challenge for concrete technology: achieving the mechanical performance and durability required for modern infrastructure while simultaneously reducing the environmental impacts associated with conventional binder systems. In this context, sustainable concrete development increasingly relies on reducing the overall cement content, lowering the clinker factor through partial replacement with supplementary cementitious materials (SCMs), valorizing industrial and agricultural by-products, and improving the efficiency and circularity of material utilization. Such approaches can reduce the demand for virgin raw materials and the energy and emissions associated with clinker production while potentially maintaining or enhancing concrete performance through physicochemical and microstructural mechanisms such as pozzolanic reactions, latent hydraulic activity, filler effects, and pore-structure refinement [4–6].

Self-compacting concrete (SCC) is an advanced concrete technology that flows and consolidates under its own weight without external vibration while remaining stable against segregation and bleeding [7]. Its performance depends on a carefully balanced rheology that provides filling ability, passing ability and segregation resistance, allowing it to flow through complex formwork and congested reinforcement without blocking [8,9]. Eliminating vibration reduces the need for compaction equipment and skilled labor and enables faster placement [10], while complete filling of intricate formwork minimizes casting defects such as honeycombing and voids [11]. These advantages are particularly relevant for heavily reinforced members, thin sections, precast components and infrastructure where conventional placement is difficult [12].

Despite these advantages, SCC presents a distinctive sustainability challenge because the high powder or binder contents needed for stable self-compaction [13,14] usually rely on Portland cement, raising embodied energy and carbon emissions [15,16]. Reducing the cement content is not straightforward, since changes in the powder fraction directly affect rheology: too little powder reduces cohesion, whereas excessive powder raises viscosity and water demand. Low-carbon SCC therefore requires optimization of the entire particulate system, including particle size distribution, packing density and compatibility with chemical admixtures [17,18], and replacement materials must not compromise strength or durability, which depend on their composition, fineness, reactivity and dosage [19]. The development of low-carbon SCC is thus a multi-objective mixture-design problem [20], which has stimulated research into SCC incorporating SCMs, industrial by-products and waste-derived powders, supported by optimized particle packing and admixture systems [21,22].

Granite powder (GP) is a promising waste-derived material for sustainable SCC. Granite cutting and processing generate large quantities of fine residues that create disposal problems when improperly managed [23,24]; this is a global issue, since the stone industry produces about 68 million tons of processed products annually and its fine waste amounts to millions of tons per year [25]. Incorporating these residues into concrete converts a low-value waste into a functional constituent, with the appropriate application depending on particle size, mineralogy and fineness [26,27]. GP contributes mainly through filler and particle-packing effects and by providing nucleation sites for hydration products, whereas any pozzolanic contribution depends on its mineralogy and should not be assumed universally [28]. Because the powder fraction controls the yield stress, viscosity and segregation resistance of SCC, appropriately proportioned GP can contribute to the powder system without compromising filling and passing ability [29,30]. However, its performance is dosage-dependent: favorable results have been reported at approximately 10% cement replacement and at 20–60% aggregate substitution [23,29], whereas higher contents tend to reduce workability and strength [25].

Ground granulated blast furnace slag (GGBFS), a glassy by-product of iron and steel manufacturing, is one of the most widely used low-carbon SCMs [31]. Replacing OPC with GGBFS reduces clinker demand, energy consumption and greenhouse gas emissions [32,33], and its latent hydraulic and pozzolanic reactions produce additional C-S-H-type hydration products that refine the pore structure and improve resistance to chloride ingress, sulfate attack and alkali–silica reaction, although carbonation resistance can be lower at high slag contents [31,34–37]. However, high slag contents can slow early-age hydration and strength development, particularly at low curing temperatures [38], and modify workability, setting and hydration kinetics [39,40]. The optimum GGBFS content must therefore be established by balancing fresh-state rheology, early- and later-age strength, durability and environmental performance.

The versatility of GGBFS has been demonstrated across a wide range of building composites. In plain and pumpable concrete, replacing 30–50% of the cement with GGBFS improved flowability and pumpability, with peak 28- and 56-day strengths at about 40% replacement despite lower early-age strength [41], while nano-sized GGBFS at 8% replacement gave strength comparable to that of the control concrete [42]. In lightweight concrete, up to 40% GGBFS increased the compressive, flexural and splitting tensile strengths of foamed concrete while reducing its porosity, water absorption and thermal conductivity [43]; GGBFS has also been used to produce cold-bonded lightweight aggregates for high-strength lightweight concrete of 37.2 MPa at a density of about 1846 kg/m^3 [44], and GGBFS-based lightweight geopolymer concrete reduced embodied carbon by 69–77% [45]. In variatropic concrete produced by vibrocentrifugation, which has a layered structure with a dense outer layer [46,47], replacing 10–50% of the cement with mechanically activated slag increased the integral compressive strength, with an optimum at 40% [48]. In geopolymer and alkali-activated systems, adding 40% GGBFS to fly ash-based geopolymer concrete increased the 91-day compressive strength by 37% relative to cement concrete [49], and ambient-cured one-part alkali-activated self-consolidating concrete based mainly on slag reached up to about 50 MPa at 90 days [50]. GGBFS also lowers the heat of hydration, which is important for massive elements: 60% replacement reduced the cumulative heat release by 36% at 20 °C [51], high-volume replacement reduced the hydration temperature rise of a 1.5 × 1.5 × 2.5 m concrete block by 11.3 °C [52], and thermal modelling of mass concrete containing 50% GGBFS reproduced measured peak temperatures within about 2% [53]. These studies show that GGBFS is beneficial across concrete types, but that its optimum content and early-age penalty depend strongly on the matrix in which it is used.

Combining GP and GGBFS is therefore attractive because their roles are expected to be complementary: GP contributes mainly through particle packing and matrix densification, improving the powder system's particle-size distribution and reducing voids, while GGBFS drives hydration and microstructural refinement while directly displacing clinker [41,54]. At optimized proportions this can produce a more balanced binder–powder system than relying on either material alone, and may offset the drawbacks of using each in isolation—excessive GP raising water demand and reducing workability and strength because of its low reactivity, and high GGBFS replacement delaying early hydration under unfavorable curing. The central research question is therefore not whether each material works individually, but whether their complementary physical and chemical roles can be balanced to meet SCC's flowability, passing, and segregation requirements together with adequate strength and durability, while maximizing the environmental benefit of cement reduction and waste valorization. That environmental benefit is not equivalent for the two materials, however. GGBFS offers the stronger, more consistently quantified carbon reduction because it directly displaces clinker—reported reductions include up to 47.5% in greenhouse gas emissions under favorable supply conditions [55], and 17% in the overall environmental impact of

slag-based cement, with further reductions in global warming potential, abiotic depletion, and energy demand at high replacement levels [56]. Evidence for GP is less extensive but still meaningful: its main benefit is valorizing granite waste and reducing virgin-resource demand, and mechanically activated (ground) GP has been shown to act as an effective filler, giving higher strength than unprocessed GP while offering carbon savings [57]. Together, the two materials offer a broader sustainability strategy than either alone—with GGBFS reducing clinker-related emissions directly and GP valorizing an abundant mineral residue and improving powder-fraction efficiency [55,57]. Prior studies combining GGBFS with granite powder in alkali-activated binders or with waste glass powder in concrete support the case for resource-efficient binder design [58,59].

Table 1 summarizes the main directions of previous research related to the present study, together with their main findings and their limitations with respect to the aim of this work.

Table 1. Summary of previous research directions related to the present study.

Research Direction	Representative Studies	Main Findings	Limitations Relative to the Present Study
Recipe and technological factors of SCC (powder content, packing, superplasticizer)	[9,13,14,17,21]	A high powder content is required; packing-based design and PCE dosage control filling ability, passing ability and stability	Mostly cement-rich systems; clinker reduction rarely optimized together with rheology
SCC with SCMs and waste-derived powders	[15,16,19,20,22,40]	SCMs and waste powders can reduce CO_2 emissions while maintaining SCC performance at optimized contents	Mostly single additions; embodied carbon seldom linked to strength development and microstructure
GP in SCC and other concretes	[23–30,57]	GP acts mainly as a filler; favorable at about 10% cement replacement; higher contents reduce workability and strength	Low reactivity; rarely combined with a reactive SCM in SCC
GGBFS in plain, pumpable and self-compacting concrete	[31,34–39,41,42,60]	Improves workability, later-age strength and durability; slows early strength gain; optimum content of about 30–50%	Early-age strength penalty; combination with inert fillers in SCC rarely studied
GGBFS in lightweight and variatropic concrete	[43–48]	Higher strength, lower porosity and thermal conductivity; optimum content of about 40% in vibrocentrifuged concrete	Different compaction technology and matrix; not directly transferable to SCC
GGBFS in geopolymer and alkali-activated concrete	[45,49,50,58]	Higher strength (up to +37% at 91 days) and denser matrix	Requires alkaline activators; not a direct route for partial OPC replacement
Combined GP and GGBFS (or GP with active admixtures)	[54,58,61]	Inert GP and active mineral admixtures can act complementarily in mortar and conventional concrete	No integrated assessment of fresh, mechanical, durability, microstructural and embodied-carbon performance of SCC

As Table 1 shows, these research directions have developed largely in parallel, and the combined use of GP and GGBFS in SCC has received comparatively little systematic attention: prior work has examined GP as a mineral addition and GGBFS as an SCM largely separately, with limited focus on how their combination balances fresh-state requirements against hardened performance. This matters because reducing OPC in SCC cannot be judged on strength alone—replacement materials must also preserve the flow and passing characteristics needed for congested reinforcement without compromising stability—and recent work on blended SCC systems has emphasized assessing fresh properties, mechanical performance, durability, and environmental impact together rather than in isolation. This study therefore provides an integrated evaluation of SCC incorporating GP and GGBFS as combined partial OPC replacements, assessing fresh-state behavior (slump flow and J-ring), hardened performance (compressive strength, splitting tensile strength and depth of water penetration), microstructure (XRD and SEM/EDX), and environmental performance (embodied carbon and strength per unit of embodied carbon), with particular attention to how the two materials' differing particle size, packing, reactivity, and water demand interact. Because the GP:GGBFS mass ratio was fixed at 1:2 in all blended mixtures, the study evaluates the combined binder system rather than the separate contribution of each material. The aim is to identify a balanced GP–GGBFS replacement strategy that meets SCC's functional requirements, delivers adequate mechanical performance and improved resistance to water penetration, and reduces the embodied carbon of cement-intensive mixtures.

2. Materials and Methods

2.1. Cement

All SCC mixtures were prepared using ordinary Portland cement (ASTM C150 [62] Type I) from Najran Cement Company (Najran, Saudi Arabia) as the main cementitious material. The cement was selected as the reference binder against which the partial replacement effects of GP and GGBFS were evaluated. Its chemical composition, determined by XRF, is given in Table 2: the cement consists mainly of CaO (61.82%) and SiO_2 (20.33%), with 4.89% Al_2O_3, 4.28% Fe_2O_3 and 2.92% SO_3, and has a loss on ignition of 1.47% and a residue of 5.8% on the 45 µm sieve.

Table 2. Chemical composition of OPC, GP and GGBFS (wt.%).

Material	SiO_2	CaO	Al_2O_3	Fe_2O_3	MgO	MnO	SO_3	Na_2O	K_2O	Cl	TiO_2	LOI
OPC	20.33	61.82	4.89	4.28	2.59	–	2.92	0.10	0.75	0.02	–	1.47
GP	70.55	1.00	12.39	3.51	–	–	0.06	4.97	6.27	–	0.29	0.67
GGBFS	32.49	37.40	17.86	0.84	8.24	0.07	0.64	0.47	0.42	–	–	0.80

2.2. Water and Superplasticizer

Potable water was used for mixing and curing throughout the experimental program. The water-to-binder ratio was controlled carefully because relatively small variations in water content can substantially affect the rheological stability and fresh-state performance of SCC. In addition to governing cement hydration, the available mixing water influences particle dispersion, paste viscosity, and the balance between flowability and segregation resistance. A polycarboxylate ether (PCE)-based high-range water-reducing admixture, Glenium 51, manufactured by BASF (Ludwigshafen, Germany), was employed to obtain the required flowability while maintaining a relatively low water-to-binder ratio. PCE-based superplasticizers promote dispersion of cementitious particles through steric and electrostatic effects, thereby reducing yield stress and improving flow without requiring additional mixing water. This function is particularly important in SCC, where high deformability must

be achieved without compromising stability or increasing the risk of segregation. The specific gravity of the Glenium 51 used in this study was 1.07, according to the manufacturer's specifications. The admixture is classified as a Type F high-range water-reducing admixture.

2.3. Aggregates

Unlike conventional concrete, SCC relies on a carefully balanced aggregate skeleton and a sufficiently cohesive paste phase to achieve high deformability while avoiding segregation and blocking. The distribution of coarse and fine particles is particularly important because variations in aggregate content and grading modify interparticle friction, paste demand, and the flow resistance of the mixture. In addition, the fine aggregate-to-total aggregate (FA/TA) ratio affects the rheological response of SCC. An excessively low FA/TA ratio may provide insufficient mortar to fill the voids between coarse particles, whereas an excessively high ratio increases the specific surface area of the aggregate skeleton and consequently the paste demand. Appropriate aggregate proportioning is therefore essential for achieving the required balance between flowability, viscosity, and passing ability.

2.3.1. Coarse Aggregate

Crushed limestone obtained from local quarries in Najran and supplied by Asalat Aljazira Company (Najran, Saudi Arabia) was used as the coarse aggregate in all mixtures. The aggregate had a maximum size of 19 mm, with 100% passing the 19 mm sieve and 92% passing the 12.5 mm sieve, and was selected for its consistent quality and grading. Its particle-size distribution was determined by sieve analysis and is presented in Figure 1a. The grading was controlled to provide an appropriate aggregate skeleton while limiting excessive coarse-particle concentration, which could increase interparticle friction and resistance to flow in SCC. The specific gravity and water absorption of the coarse aggregate were 2.60 and 1.50%, respectively, as determined in accordance with ASTM C127 [63]. The particle-size distribution was evaluated according to ASTM C136/C136M [64]. These properties were incorporated into the mixture calculations to ensure accurate aggregate volume, moisture correction, and effective water-to-binder ratio.

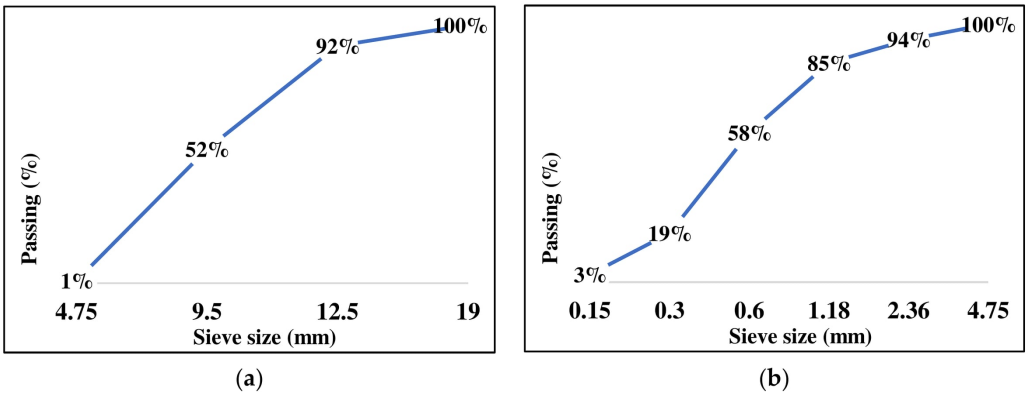


Figure 1. Particle size distribution of the aggregates: (**a**) coarse aggregate; (**b**) fine aggregate.

2.3.2. Fine Aggregate

Natural dune sand was used as the fine aggregate, with a specific gravity of 2.60 and water absorption of 0.57%. Its particle-size distribution, determined by sieve analysis, is presented in Figure 1b. The grading extends from 4.75 to 0.15 mm, with approximately 3% passing the 0.15 mm sieve. The fine aggregate grading contributes to the packing of the granular skeleton and influences mortar volume, paste demand, and the rheological characteristics of the SCC mixtures. The specific gravity and water absorption of the fine

aggregate were determined in accordance with ASTM C128 [65], while sieve analysis was conducted according to ASTM C136/C136M. The measured absorption and moisture condition of the fine aggregate were considered during mixture proportioning to maintain accurate control of the effective water-to-binder ratio.

2.4. Cement Replacement Materials

2.4.1. Granite Powder (GP)

The GP used in this study was collected as a waste by-product from granite cutting and polishing factories in Najran, Saudi Arabia. During the cutting of granite blocks into slabs and tiles, water is continuously applied to the cutting blade for cooling and dust suppression, producing a slurry of fine stone dust suspended in water (Figure 2a). This slurry flows along a collection channel (Figure 2b) toward a filter unit (Figure 2c), where the water is separated from the dust: the filtered water is recycled back into the cutting process, while the granite dust is retained and collected separately as filter cake. The as-received GP used in this study was collected in bulk directly from the factories' filter units. The collected GP was first oven-dried at 105 °C for 2 h to remove residual moisture from the wet-cutting process. The dried material was then ground using a ball mill for 10 min to break up the agglomerated lumps formed during drying, yielding a free-flowing fine powder ready for use as a partial cement replacement.

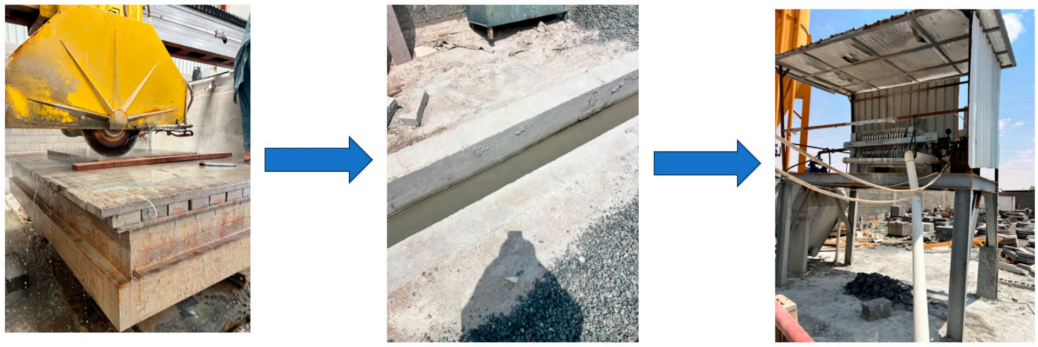


Figure 2. Granite cutting and GP collection: (**a**) block cutting with water cooling; (**b**) slurry collection channel; (**c**) filter unit.

The chemical composition of GP (Table 2), obtained by XRF, is dominated by SiO_2 (70.55%), with substantial Al_2O_3 (12.39%), K_2O (6.27%) and Na_2O (4.97%) contents, reflecting a quartzo-feldspathic granitic origin; the low LOI (0.67%) indicates minimal hydrous or carbonate content. The specific gravity of GP was 2.6. The particle size distribution (Figure 3), measured by laser diffraction (Mastersizer 2000 with a Scirocco 2000 dry dispersion unit; Malvern Instruments, Malvern, UK), shows a fine powder with D_{10}, D_{50} and D_{90} values of approximately 6, 18.5 and 43.5 µm, respectively. The XRD pattern (Figure 4) exhibits sharp quartz reflections at about 20.9° and 26.7° 2θ, the latter being the most intense, along with reflections at about 27.5–28.0° 2θ attributable to feldspar, confirming GP is predominantly crystalline rather than amorphous. SEM images (Figure 5) reveal angular, irregularly shaped particles with sharp fracture surfaces typical of mechanically crushed rock, while EDX (Figure 6) corroborates the XRF results, showing O and Si as the dominant elements, together with minor Al, Na, K and Fe and traces of Cu and Zn (<1 wt.%).

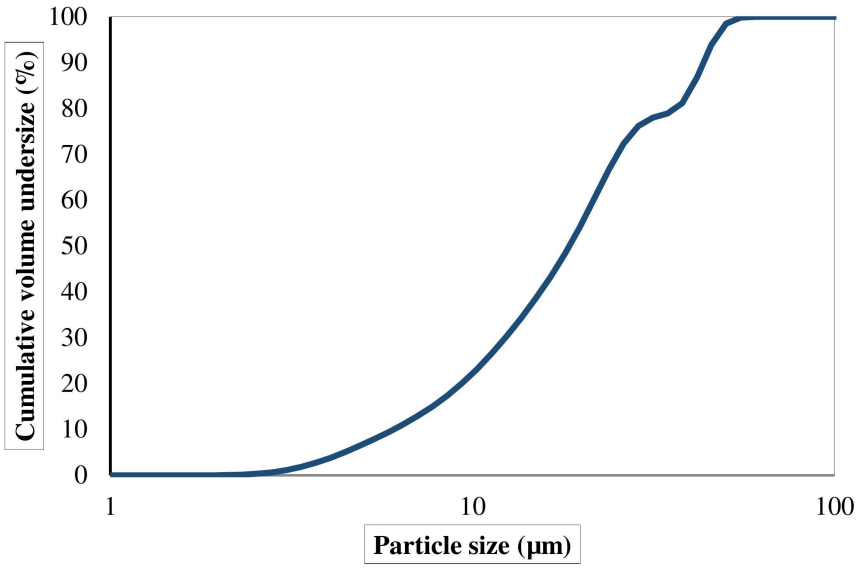


Figure 3. Particle size distribution of GP.

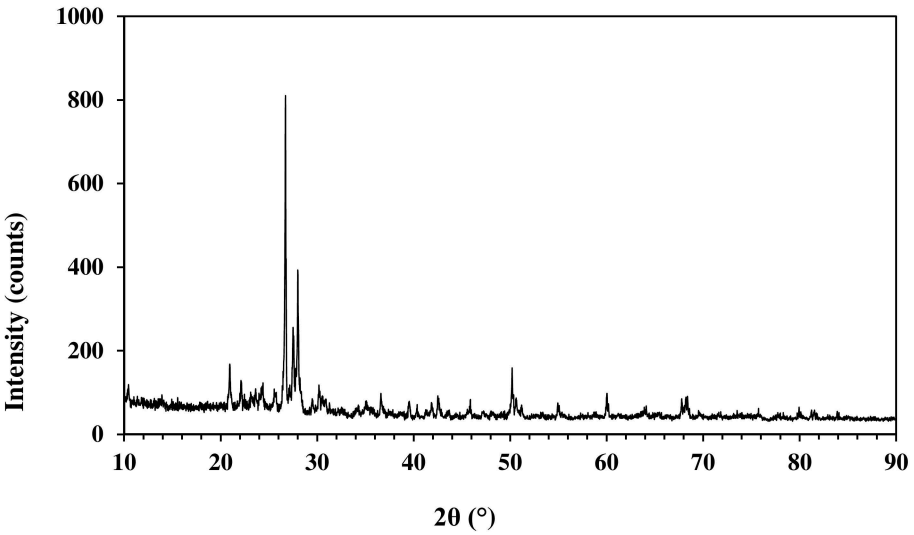
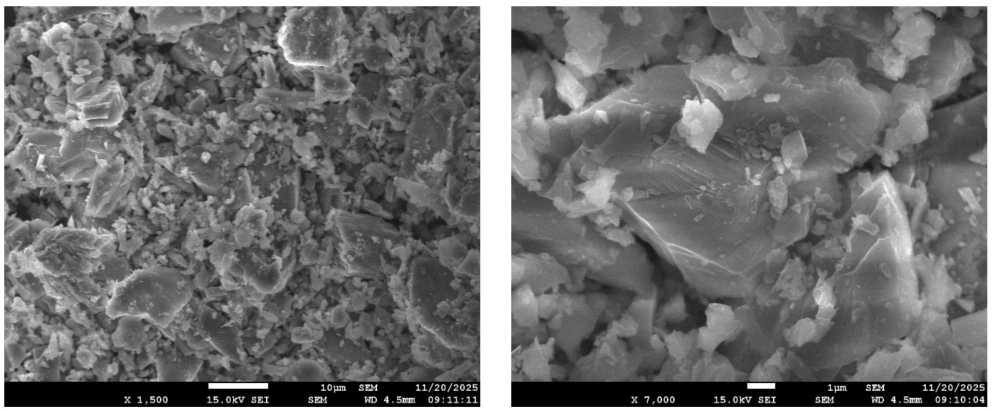
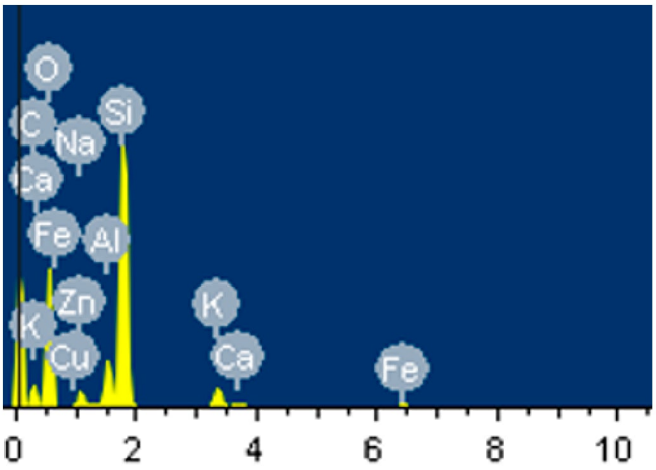


Figure 4. XRD pattern of GP.



(**a**) (**b**)

Figure 5. SEM images of GP at (**a**) ×1500 and (**b**) ×7000 magnification.



Element	Weight (%)
C K	13.57
O K	52.47
Na K	2.02
Al K	3.73
Si K	22.85
K K	2.48
Ca K	0.27
Fe K	1.08
Cu K	0.87
Zn K	0.67

Figure 6. EDX spectrum and elemental composition (wt.%) of GP.

2.4.2. Ground Granulated Blast Furnace Slag (GGBFS)

GGBFS, supplied by Al Rashed Cement Company (Najran, Saudi Arabia), was used in this study. The material had a specific surface area of 4400 cm^2/g, with specific gravity 2.8 and a residue retained on the 45 µm sieve of ≤5.0%; its chemical composition is presented in Table 2.

2.5. Experimental Program

The experimental program is summarized in Figure 7. The SCC mixtures were proportioned following the EFNARC guidelines for SCC [66] using an absolute-volume-based mix design approach. The proportions of cementitious materials, water, aggregates, and superplasticizer were selected to achieve the required balance between flowability, viscosity, passing ability, and segregation resistance. The total binder content was maintained at 514.1 kg/m^3 for all mixtures, while the water content was kept constant at 205.6 kg/m^3, corresponding to a water-to-binder ratio of approximately 0.40. The coarse aggregate content was also maintained at 833 kg/m^3, whereas the fine aggregate and superplasticizer contents were adjusted as required to accommodate the changes in binder composition and achieve the targeted fresh-state performance. The superplasticizer dosage required to achieve the target flow increased with the replacement level, from 0.64% of the binder mass in the control mixture to 0.69%, 0.97% and 1.47% in GP5S10, GP10S20 and GP15S30, respectively. This equal-workability approach, in which the superplasticizer dosage is adjusted to reach a target slump-flow class, is standard practice in SCC design, because a fixed dosage would have produced mixtures that were either not self-compacting or prone to segregation, and therefore not comparable. The fine aggregate content was reduced by only 1.2%, 2.4% and 4.0% in GP5S10, GP10S20 and GP15S30, respectively, solely to compensate, on an absolute-volume basis, for the lower specific gravities of GP (2.6) and GGBFS (2.8) relative to cement and for the higher superplasticizer volume, so that each mixture yielded approximately 1 m^3 with the same binder, water and coarse aggregate contents. The calculated mixture proportions were based on the specific gravities and moisture-related properties of the constituent materials described previously. Four SCC mixtures were prepared. The control mixture (CO) contained 100% OPC as the cementitious binder, with no GP or GGBFS replacement. Three additional mixtures were produced by progressively increasing the combined replacement of OPC with GP and GGBFS. The first modified mixture, GP5S10, incorporated 5% GP and 10% GGBFS as partial replacements of OPC, corresponding to a total binder replacement level of 15%. The second mixture, GP10S20, contained 10% GP and 20% GGBFS, resulting in a total OPC replacement of 30%. The third mixture, GP15S30,

incorporated 15% GP and 30% GGBFS, corresponding to a total replacement level of 45%. The GP:GGBFS mass ratio of 1:2 was selected so that the predominantly inert GP was limited to 15% of the binder at the highest replacement level, close to the level of about 10% reported as favorable for GP as a cement replacement [29], while the reactive GGBFS supplied the larger share of the replacement, within the range of 30–50% commonly reported as optimal [41]. Because this ratio was fixed, the study was designed to evaluate the combined binder system at increasing replacement levels rather than the separate contribution of each material. In all modified mixtures, the combined mass of OPC, GP, and GGBFS was maintained at 514.1 kg/m^3 to isolate the effect of the replacement level and composition of the binder system. The mixture proportions of the four mixtures are given in Table 3. This systematic increase in the GP–GGBFS replacement level was adopted to evaluate its effect on the fresh, mechanical, durability, and environmental performance of SCC while maintaining a consistent overall binder and water content.

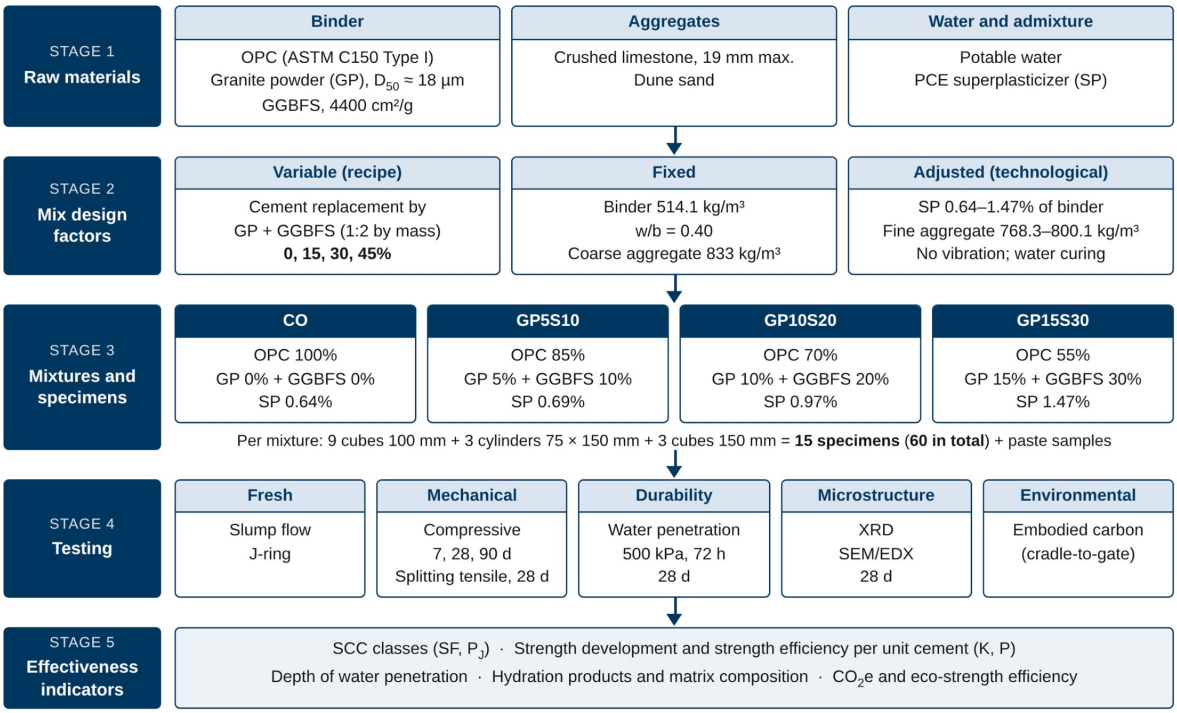


Figure 7. Flowchart of the experimental program.

Table 3. Mix proportions of the SCC mixtures (kg/m^3).

Mix	Code	Cement	GP	GGBFS	Coarse Aggregate	Fine Aggregate	Water	SP	SP (% of Binder) [1]
Control	CO	514.10	–	–	833	800.10	205.6	3.30	0.64
5% GP + 10% GGBFS	GP5S10	436.98	25.71	51.41	833	790.55	205.6	3.56	0.69
10% GP + 20% GGBFS	GP10S20	359.87	51.41	102.82	833	781.25	205.6	5.01	0.97
15% GP + 30% GGBFS	GP15S30	282.76	77.12	154.23	833	768.34	205.6	7.58	1.47

[1] Superplasticizer dosage expressed as a percentage of the total binder mass.

2.6. Mixing, Casting and Curing

The concrete mixtures were prepared using a controlled mixing procedure to ensure uniform dispersion of the cementitious materials, aggregates, water, and superplasticizer. The constituent materials were first introduced into the mixer (a 120 L drum-type concrete mixer) and dry-mixed to obtain a uniform distribution of the solid particles. Water was then added gradually, followed by the required dosage of the polycarboxylate-based superplasti-

cizer. Mixing was continued until a homogeneous SCC mixture with uniform consistency was obtained. Particular care was taken to maintain the designed water-to-binder ratio and superplasticizer dosage for each mixture. The mixing and specimen preparation procedures were conducted in accordance with the relevant provisions of ASTM C192/C192M [67] for the preparation and curing of concrete specimens under laboratory conditions. For each mixture, 9 cube specimens (100 × 100 × 100 mm; three per testing age) were prepared for compressive strength evaluation at 7, 28, and 90 days. In addition, three cube specimens (150 × 150 × 150 mm) were cast for the water penetration test at 28 days. Three cylindrical specimens with dimensions of 75 mm in diameter and 150 mm in height were also prepared for the splitting tensile strength test at 28 days. The molds were cleaned and lightly coated with a suitable release agent before casting. The fresh SCC was carefully poured into the molds without mechanical vibration or external compaction, allowing the concrete to fill the molds and consolidate under its own weight. This procedure is consistent with the fundamental placement principle of SCC and avoids introducing segregation or altering the self-compacting characteristics of the mixtures through external vibration. Following casting, the exposed surfaces were leveled and protected against moisture loss. The specimens remained in their molds for approximately 24 h at laboratory conditions before demolding. After demolding, all specimens were immediately transferred to a water-curing tank and cured continuously until the designated testing ages. The curing procedure was controlled to minimize variations in moisture and temperature among the mixtures and to provide comparable hydration conditions throughout the experimental program. Specimen preparation, demolding, and curing were conducted with reference to ASTM C192/C192M procedures for concrete specimen preparation and curing.

2.7. Test Methods

2.7.1. Slump Flow

The slump-flow test was performed in accordance with BS EN 12350-8 [68] to evaluate the filling ability and flowability of the fresh SCC mixtures. A standard Abrams cone with a 200 mm bottom diameter, 100 mm top diameter, and 300 mm height was placed on a smooth, level, non-absorbent surface and filled with SCC without mechanical compaction. The cone was then lifted vertically, allowing the concrete to spread freely under its own weight. After the flow had ceased, the final spread diameter was measured in two approximately perpendicular directions, and the average of the two measurements was reported as the slump-flow diameter. The test arrangement and equipment are presented in Figure 8a, while the resulting spread of the concrete is shown in Figure 8b. A higher slump-flow value indicates greater deformability and filling ability, provided that the mixture remains stable and free from visible segregation. The mixtures were classified using the slump-flow classes of the European SCC guidelines (SF1: 550–650 mm; SF2: 660–750 mm; SF3: 760–850 mm) [66].

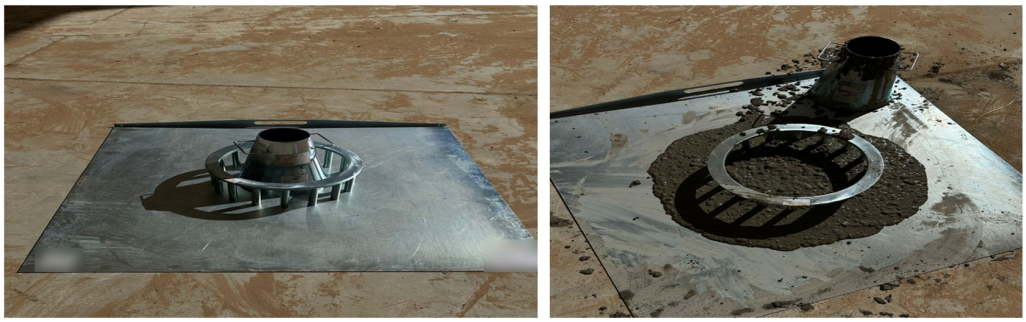


(a) (b)

Figure 8. Slump-flow test: (**a**) apparatus; (**b**) measurement of the slump-flow spread.

2.7.2. J-Ring Test

The J-ring test was conducted in accordance with BS EN 12350-12 [69] to assess the passing ability of the SCC mixtures through closely spaced reinforcement. The test employed the same Abrams cone used for the slump-flow test (200 mm bottom diameter, 100 mm top diameter and 300 mm height), together with a J-ring fitted with vertical steel bars. The cone was positioned centrally within the J-ring and filled with fresh SCC without compaction. After the cone was lifted vertically, the concrete flowed freely through the bars until the spread had stabilized. The blocking step (P_J) was then determined from the difference in concrete surface height between the centre of the spread and the mean of four positions immediately outside the bars. A lower P_J indicates less blocking and therefore better passing ability. The test setup and accessories are shown in Figure 9a, and the resulting concrete spread is presented in Figure 9b.



(a) (b)

Figure 9. J-ring test: (**a**) apparatus; (**b**) concrete spread after the test.

2.7.3. Compressive and Splitting Tensile Strength

The compressive strength of the SCC mixtures was determined at 7, 28, and 90 days using 100 × 100 × 100 mm cubic specimens. For each mixture and testing age, three specimens were tested, and the average compressive strength was calculated from the individual measurements. Before testing, the specimens were removed from the curing tank and their surfaces were cleaned and prepared to ensure uniform contact with the loading platens. The cubes were positioned centrally in the testing machine (2000 kN capacity; Matest S.p.A., Treviolo, Italy) and subjected to a continuously increasing axial compressive load until failure. The compressive strength was calculated as the maximum applied load divided by the loaded cross-sectional area. The test was conducted in accordance with BS EN 12390-3 [70], which specifies the procedures for determining the compressive strength of hardened concrete. The development of compressive strength with curing age was used to assess the effect of GP and GGBFS replacement on both early-age and later-age strength development. The 7-day results provided an indication of early strength development, whereas the 28- and 90-day results were used to evaluate the progressive contribution of binder hydration and pozzolanic/latent hydraulic reactions to the hardened matrix. The compression testing machine used is shown in Figure 10.

The splitting tensile strength was evaluated at 28 days using cylindrical specimens measuring 75 mm in diameter and 150 mm in height. Three specimens were tested for each mixture. Prior to testing, the specimens were removed from water curing and prepared for loading. Each cylinder was positioned horizontally between the compression platens of the testing machine, with the load applied continuously along two diametrically opposite lines until failure. The resulting tensile stress generated perpendicular to the loading plane produced a characteristic longitudinal splitting failure. The splitting tensile strength was determined from the maximum applied load using the standard relationship between

the failure load, specimen diameter, and specimen length. The test was performed in accordance with ASTM C496 [71], which specifies the method for determining the splitting tensile strength of hardened concrete. The obtained values were used to assess the influence of combined GP and GGBFS replacement on the tensile resistance and cracking-related behavior of the SCC mixtures.

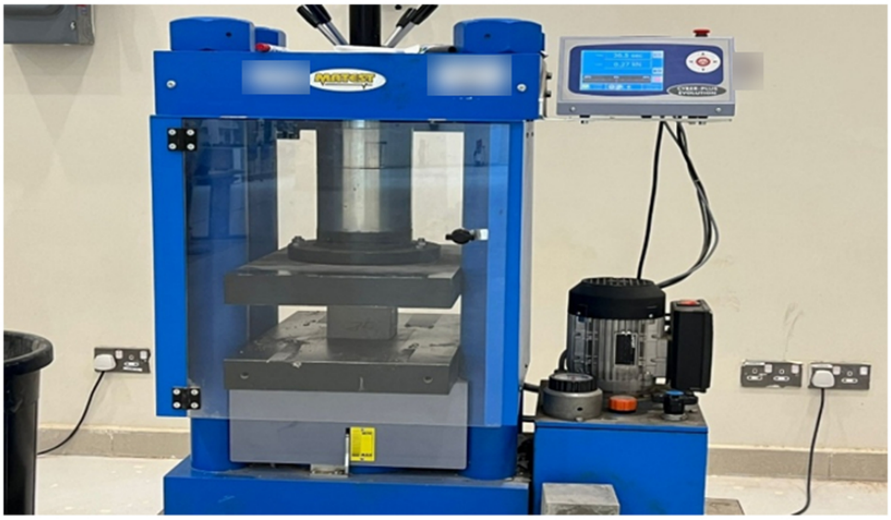


Figure 10. Compression testing machine used for the cube specimens.

2.7.4. Specific Strength Indices

The contribution of GP and GGBFS to the compressive strength of the SCC mixtures was quantified using the specific strength ratio (R), the pozzolanic strength contribution (R_p), the strength efficiency index (K), and the pozzolanic contribution percentage (P), following the approach of Yu et al. [72]. This method separates the compressive strength of a blended mixture into two components: the strength attributable to its cement content alone (dilution effect) and the additional strength attributable to the combined pozzolanic and filler activity of the GP–GGBFS system, expressed as:

$$R = \frac{f}{q} \tag{1}$$

$$R_p = R_m - R_c \tag{2}$$

$$K = \frac{R_m}{R_c} \tag{3}$$

$$P = \frac{R_m - R_c}{R_m} \times 100\% \tag{4}$$

where f is the compressive strength of the mixture (MPa) and q is the cement content expressed as a percentage of the total binder content (514.1 kg/m^3). R_c is the specific strength ratio of the control mixture (CO, 100% OPC, q = 100%) at a given age, and R_m is the specific strength ratio of each GP–GGBFS blended mixture (for GP5S10, GP10S20, and GP15S30, q = 85%, 70%, and 55%, respectively) at the same age. R_p represents the portion of specific strength attributable to the combined pozzolanic and filler activity of GP and GGBFS beyond simple cement dilution; K expresses the strength efficiency of the blended mixture relative to the control ($K > 1$ indicating a mixture that is more strength-efficient per unit cement than pure OPC); and P expresses this contribution as a percentage of the blended mixture's total specific strength. R and R_p are expressed in MPa per percentage point of cement (MPa/%). R, R_p, K, and P were calculated for each mixture at 7, 28, and 90 days using the corresponding compressive strength results. Because GP is predominantly

crystalline (Section 2.4.1), R_p and P capture the combined effect of the GGBFS reaction and the filler and nucleation effects of both powders; P is referred to here as the pozzolanic contribution for consistency with [72], but it is not a measure of chemical reactivity alone.

2.7.5. Depth of Water Penetration

The resistance of the SCC mixtures to water penetration was evaluated at 28 days in accordance with BS EN 12390-8 [73]. Three cube specimens measuring 150 × 150 × 150 mm were tested for each mixture. After completion of the curing period, the specimens were placed in a water-permeability apparatus (model C435; Matest S.p.A., Treviolo, Italy) and subjected to a water pressure of 500 kPa (5 bar) applied to one surface of the specimen for 72 h, as specified in EN 12390-8, allowing water to penetrate into the concrete under controlled pressure. At the end of the test, the specimens were removed from the apparatus and split perpendicular to the surface subjected to water pressure. The maximum depth of water penetration was then measured and recorded for each specimen. The average penetration depth of the three specimens was used as the representative value for each mixture. A lower penetration depth indicates greater resistance to water ingress and reflects a denser and less permeable concrete matrix. The test results were used to evaluate the influence of the combined GP and GGBFS replacement on the water penetration resistance of the developed SCC mixtures.

2.7.6. Microstructural Analysis

The microstructural evolution of the hardened cement pastes was investigated by XRD. Paste specimens were cast for the control and each GP–GGBFS blended mixture and cured for 28 days. At the end of the curing period, the hardened paste samples were crushed and ground into powder for XRD analysis. Patterns were acquired on a PANalytical X'Pert PRO diffractometer (PANalytical, Almelo, The Netherlands), equipped with a PW3050/60 Bragg–Brentano θ/θ goniometer (240 mm radius) and a PW3071/xx sample bracket, using Cu-Kα radiation (Kα1 = 1.54060 Å, Kα2 = 1.54443 Å, Kα2/Kα1 ratio = 0.5) generated at 45 kV and 40 mA. A fixed divergence slit of 1.0° and a 0.1 mm receiving slit were used, with a 10 mm irradiated specimen length. Scans were collected in continuous mode over a range of 5–90° 2θ (plotted over 5–60° 2θ for clarity), with a step size of 0.01° 2θ and a counting time of 0.45 s per step, at a measurement temperature of 25 °C, without sample spinning or an incident-beam monochromator. SEM/EDX analysis was carried out on fractured fragments taken from the core of the 28-day concrete specimens. Micrographs were acquired with a JEOL scanning electron microscope (JEOL Ltd., Tokyo, Japan) in secondary-electron imaging (SEI) mode at an accelerating voltage of 10 kV and a working distance of 4.5 mm. To allow direct comparison between mixtures, representative images were recorded under identical conditions at ×5000 to show the overall matrix and at ×30,000 to resolve the hydration products. Elemental composition was determined using the attached EDX detector at 15 kV. For each mixture, five EDX analyses were acquired on a representative region of the matrix (two point analyses, two partial-area scans and one full-field area scan) and quantified with the INCA software (Oxford Instruments, Abingdon, UK), with all detected elements analyzed and normalized to 100 wt.%. Results are reported as the average of the five analyses and the Ca/Si and Ca/Al mass ratios were calculated from the average weight percentages of each mixture.

2.7.7. Embodied Carbon Assessment

To assess the environmental performance of the developed SCC mixtures, a simplified cradle-to-gate life cycle assessment (LCA) was performed, focusing on the embodied carbon associated with partial cement replacement by GP and GGBFS. For each mixture, the total

embodied carbon per cubic meter of concrete was determined through a mass-weighted summation of all constituent materials:

$$CO_2e = \sum (W_i \times CO_{2,i}) \quad (5)$$

where W_i is the mass of constituent i in one cubic meter of concrete (kg/m^3) and $CO_{2,i}$ is the corresponding embodied carbon factor of that constituent ($kgCO_2e/kg$). Emission factors for cement, coarse aggregate, fine aggregate, water, superplasticizer and GGBFS were taken from the literature [74–78] and are listed in Table 4. For GP, an embodied carbon factor of 0.2527 $kgCO_2e/kg$ was derived under the waste-valorization system boundary defined by ISO 14044 [79], based on the electricity demand of the two processing steps involved in preparing the material: oven drying at 105 °C, contributing 0.0506 $kgCO_2e/kg$, and grinding, contributing 0.2020 $kgCO_2e/kg$. These values were obtained by applying the carbon intensity of the Saudi electricity grid of approximately 0.55 $kgCO_2e/kWh$, which reflects a generation mix dominated by natural gas with some crude and heavy fuel oil contribution [80], to the measured electricity consumption of each step. Because GP is a waste slurry obtained at no cost from the granite-processing industry, no environmental burden was assigned to its raw-material acquisition stage; only the energy consumed during its preparation was accounted for. Because these electricity demands were measured on laboratory-scale equipment, the resulting GP factor is likely to be conservative relative to industrial-scale processing. An eco-efficiency index was further introduced to relate mechanical performance to environmental cost, expressed as the ratio of 28-day compressive strength (f_{28}) to the total embodied carbon of each mixture:

$$\text{Eco} - \text{strength efficiency} = \frac{f_{28}}{CO_2e} \quad (6)$$

Table 4. Embodied carbon factors adopted for the concrete constituents.

Material	Embodied Carbon ($kgCO_2e/kg$)	Source
Cement	0.82	[74]
Coarse aggregate	0.0459	[75]
Fine aggregate	0.0139	[76]
Water	0	[76]
Superplasticizer	0.72	[77]
GGBFS	0.155	[78]
GP	0.2527	This study

A higher value of this index (expressed in $MPa{\cdot}m^3/kgCO_2e$) reflects a mixture that delivers more compressive strength per unit of embodied carbon, indicating better carbon efficiency.

3. Results

3.1. Slump Flow

The slump flow test was conducted to evaluate the flowability of the investigated SCC mixtures incorporating different proportions of GP and GGBFS. As shown in Figure 11, the CO mixture exhibited a slump flow of 745 mm. Incorporating 5% GP and 10% GGBFS (GP5S10) resulted in a slight reduction to 737 mm, indicating that the initial replacement level had a limited effect on flowability. Increasing the replacement level to 30% in GP10S20 further reduced the slump flow to 694 mm. This reduction may be attributed to the increased proportion of fine particles and the associated changes in water demand, particle packing, and rheological behavior. Despite the relatively high fineness of GGBFS, with a specific surface area of 4400 cm^2/g, and the fine particle size distribution of GP (D50 ≈ 18 μm), the

combined effects of these materials on flowability depend on their particle characteristics, proportions, and interaction with the superplasticizer.

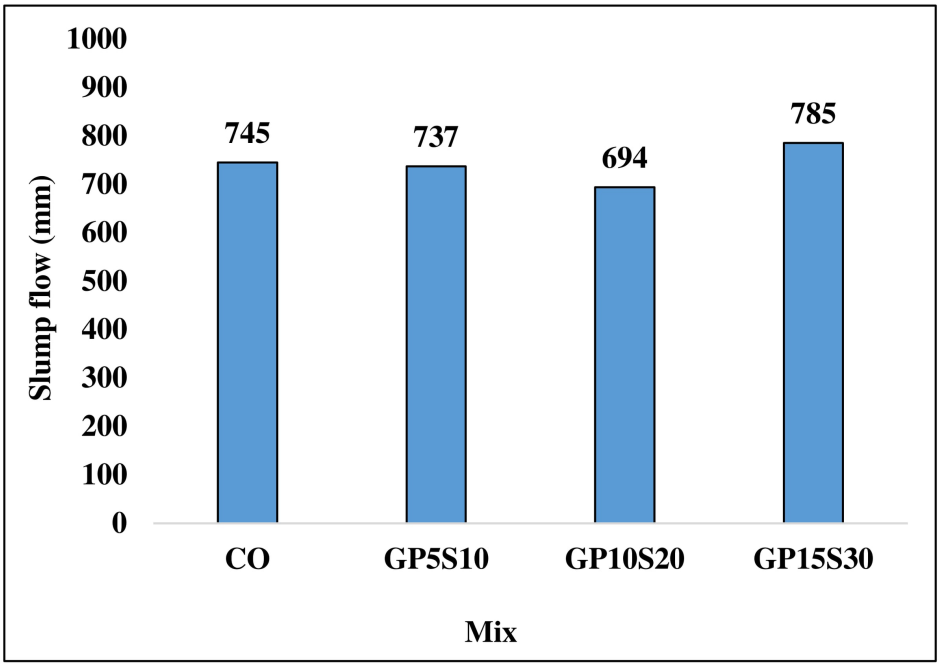


Figure 11. Slump flow of the SCC mixtures.

At the highest replacement level of 45% (GP15S30), the slump flow increased to 785 mm, exceeding that of the control mixture. This increase may be associated with the higher superplasticizer dosage (7.58 kg/m^3, i.e., 1.47% of the binder mass compared with 0.64% for CO), which enhanced particle dispersion and reduced resistance to flow. This finding highlights the importance of admixture dosage in controlling the fresh properties of SCC containing high proportions of supplementary cementitious materials. The results obtained in the current study indicate that the effect of GP and GGBFS incorporation on the flowability of SCC was not strictly proportional to the replacement level. Instead, it was governed by the combined effects of binder composition, particle characteristics, and superplasticizer dosage. The reduction in slump flow at the intermediate replacement level and the subsequent increase at the highest level suggest that the fresh behavior of these mixtures was strongly influenced by the interaction between the powder content and admixture dosage. According to the slump-flow classes of the European SCC guidelines [66], CO, GP5S10 and GP10S20 fall within class SF2 (660–750 mm) and GP15S30 within class SF3 (760–850 mm).

3.2. J-Ring Passing Ability

The J-ring test was performed to assess the passing ability of the SCC mixtures and to examine the potential blocking effect associated with the incorporation of GP and GGBFS. As shown in Figure 12, the CO mixture exhibited a blocking step (P_J) of 3.5 mm, while the incorporation of 5% GP and 10% GGBFS (GP5S10) reduced the value to 2.6 mm. Increasing the replacement level to 30% (GP10S20) resulted in a slight increase to 3.0 mm, whereas the highest replacement level of 45% (GP15S30) produced the lowest value of 2.4 mm. The relatively small variation in P_J, within a narrow range of 2.4–3.5 mm, suggests that the incorporation of GP and GGBFS caused only minor changes in the passing ability of the investigated SCC mixtures. The slight fluctuations in P_J can be attributed to the combined effects of particle packing, paste viscosity, binder composition, and superplasticizer dosage. Although fine particles can improve particle packing and contribute to a more

homogeneous paste structure, excessive powder content may increase viscosity and internal friction, thereby restricting the passage of concrete through reinforcement. These results are compared with previous studies in Section 4.1.

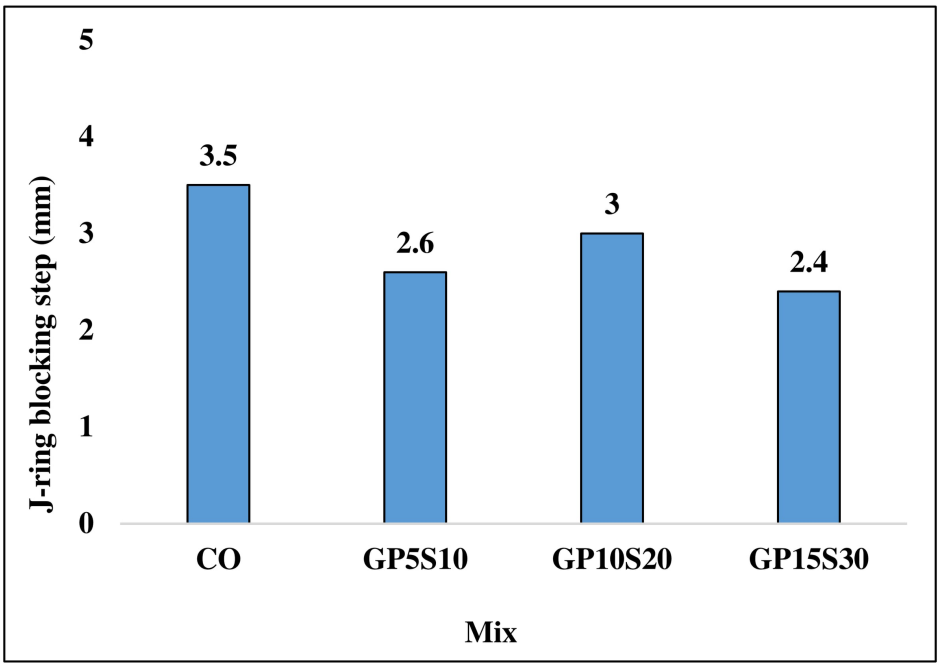


Figure 12. J-ring blocking step (P_J) of the SCC mixtures.

In the present study, the consistently low P_J values suggest that the increased fineness of GP and GGBFS did not cause substantial blocking under the tested conditions. The higher superplasticizer dosages used in the modified mixtures may also have promoted particle dispersion and reduced resistance to flow through the reinforcement. The results indicate that the investigated GP–GGBFS replacement levels maintained acceptable passing ability, with only minor variations in blocking step despite changes in binder composition and fresh-state rheology. These findings highlight the importance of considering the combined effects of powder characteristics and admixture dosage when evaluating the passing ability of SCC.

3.3. Compressive Strength

The compressive strength of the SCC mixtures at 7, 28, and 90 days is shown in Figure 13, and the corresponding mean values, standard deviations (SD) and coefficients of variation (CV) are summarized in Table 5. The CVs of the compressive strength results ranged from 3.42% to 8.51%, indicating acceptable repeatability of the test results. The control mixture (CO) achieved compressive strengths of 42.7, 56.0, and 76.7 MPa at 7, 28, and 90 days, respectively. Strength development followed distinct trends across the three ages. At 7 days, strength decreased with increasing cement replacement, most markedly at the highest replacement level (GP15S30, 45% total cement replacement), which recorded only 17.3 MPa compared with 42.7 MPa for the control. This early-age strength loss is primarily attributable to the dilution effect of the high volume of cement replaced, since cement remains the principal binding agent governing early hydration [81]. However, the 7-day strength of GP15S30 was also lower than the approximately 23.5 MPa expected from cement dilution alone (0.55 × 42.7 MPa), indicating that early hydration was further delayed. This additional delay is consistent with the slow early reaction of GGBFS [81] and may also reflect the higher superplasticizer dosage of this mixture (1.47% of the binder mass, compared with 0.64% for CO), since high dosages of PCE superplasticizers can retard early

cement hydration. By 28 days, the differences between mixtures had narrowed considerably. In particular, GP5S10 (5% GP and 10% GGBFS) reached 55.4 MPa, closely approaching the control's 56.0 MPa, indicating that at this replacement level the combined GP–GGBFS system compensated for almost all of the reduction in cement content. At 90 days, the trend shifted further: GP5S10 and GP10S20 reached 69.9 and 69.6 MPa, about 9% below the control, whereas the highest-replacement mixture, GP15S30 (15% GP and 30% GGBFS), recorded the largest strength gain of all mixtures and reached 83.8 MPa, 9.3% above the control. This marked late-age improvement reflects the continued latent hydraulic and pozzolanic reaction of GGBFS [82] with the residual cement and its hydration products, which promotes further formation of C-S-H, progressively densifying the microstructure and compensating for the early-age strength deficit caused by cement dilution. The larger late-age gain of GP15S30 compared with GP5S10 and GP10S20 is consistent with its higher GGBFS content (30% of the binder), which provides more reactive material once the early-age dilution effect has been overcome, while GP contributes mainly through particle packing. The strength development is discussed in relation to previous studies in Section 4.2, including its implications for mass concrete.

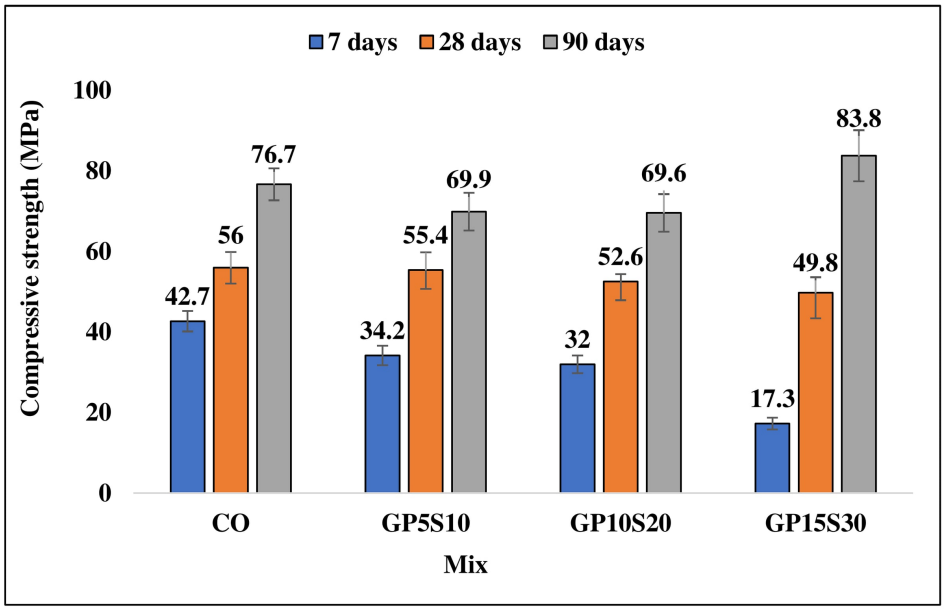


Figure 13. Compressive strength of the SCC mixtures at 7, 28 and 90 days.

Table 5. Mechanical properties and depth of water penetration of the SCC mixtures, expressed as mean ± standard deviation (SD) and coefficient of variation (CV) of three specimens.

Mix Code	Compressive Strength (7d)		Compressive Strength (28d)		Compressive Strength (90d)		Splitting Tensile Strength (28d)		Depth of Water Penetration (28d)	
	Mean ± SD (MPa)	CV (%)	Mean ± SD (MPa)	CV (%)	Mean ± SD (MPa)	CV (%)	Mean ± SD (MPa)	CV (%)	Mean ± SD (mm)	CV (%)
CO	42.7 ± 2.5	5.94	56.0 ± 3.9	6.92	76.7 ± 4.0	5.16	3.25 ± 0.09	2.66	18.0 ± 1.7	9.62
GP5S10	34.2 ± 2.4	7.10	55.4 ± 4.4	7.98	69.9 ± 4.7	6.70	3.90 ± 0.13	3.39	13.0 ± 0.0	0.00
GP10S20	32.0 ± 2.2	6.88	52.6 ± 1.8	3.42	69.6 ± 4.7	6.73	3.60 ± 0.22	6.05	10.0 ± 1.0	10.00
GP15S30	17.3 ± 1.5	8.51	49.8 ± 3.8	7.72	83.8 ± 6.4	7.58	3.70 ± 0.09	2.34	7.0 ± 1.0	14.29

3.4. Specific Strength Indices

Table 6 quantifies the trends observed in the compressive strength results by separating each mixture's strength into the portion attributable to its cement content alone (dilution effect) and the portion attributable to the combined pozzolanic and filler activity of GP

and GGBFS. The pozzolanic contribution percentage (P) derived from this table is plotted in Figure 14. For the control mixture (CO), R increased steadily from 0.427 to 0.560 to 0.767 MPa/% with age, and by definition $R_p = 0$, $K = 1.00$, and $P = 0\%$ at all ages, serving as the baseline against which the blended mixtures are compared. At 7 days, the dilution effect dominated the blended mixtures' behaviour, consistent with the pronounced early-age strength loss described above. As shown in Figure 14, GP5S10 and GP15S30 both recorded negative P values (−6.1% and −35.8%, respectively), indicating that their early strength was governed almost entirely by their reduced cement content rather than any pozzolanic contribution. GP10S20 was the exception, already showing a small positive contribution ($K = 1.07$, $P = 6.6\%$) at this age. By 28 days, all three blended mixtures had turned strongly positive, mirroring the narrowing of the strength gap seen in Figure 13. GP5S10 reached $K = 1.16$ ($P = 14.1\%$), GP10S20 reached $K = 1.34$ ($P = 25.5\%$), and GP15S30—despite having the lowest 7-day performance—recorded the highest efficiency of the three at this age ($K = 1.62$, $P = 38.2\%$), reflecting the onset of GGBFS reaction offsetting its larger cement deficit. At 90 days, GP5S10 and GP10S20 both eased slightly from their 28-day peaks ($K = 1.07$ and 1.30, $P = 6.7\%$ and 22.9%, respectively) while remaining above the control, suggesting that their contribution had begun to stabilize relative to the continuing hydration of the control's cement. GP15S30, in contrast, continued to rise sharply, reaching $K = 1.99$ and $P = 49.7\%$, the highest values recorded in the study (Figure 14). This indicates that, on a per-unit-cement basis, GP15S30 became nearly twice as strength-efficient as the control by 90 days, consistent with the sustained late-age compressive strength gain attributed to continued C-S-H formation from the reaction of GGBFS (Section 3.3).

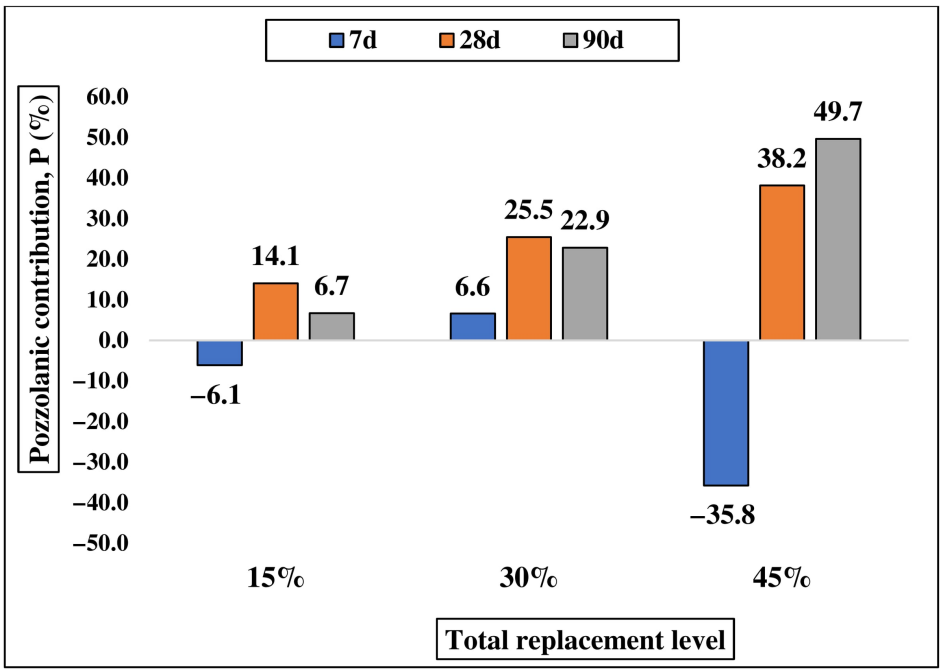


Figure 14. Pozzolanic contribution (P) of the blended mixtures at 7, 28 and 90 days.

Table 6. Specific strength indices of the SCC mixtures.

Mix	Replacement (%)	Age (Days)	f (MPa)	R (MPa/%)	R_p (MPa/%)	K	P (%)
CO	0	7	42.7	0.427	0.000	1.00	0
		28	56.0	0.560	0.000	1.00	0
		90	76.7	0.767	0.000	1.00	0

Table 6. *Cont.*

Mix	Replacement (%)	Age (Days)	f (MPa)	R (MPa/%)	R_p (MPa/%)	K	P (%)
GP5S10	15	7	34.2	0.402	−0.025	0.94	−6.1
		28	55.4	0.652	0.092	1.16	14.1
		90	69.9	0.822	0.055	1.07	6.7
GP10S20	30	7	32.0	0.457	0.030	1.07	6.6
		28	52.6	0.751	0.191	1.34	25.5
		90	69.6	0.994	0.227	1.30	22.9
GP15S30	45	7	17.3	0.315	−0.112	0.74	−35.8
		28	49.8	0.905	0.345	1.62	38.2
		90	83.8	1.524	0.757	1.99	49.7

3.5. Splitting Tensile Strength

As shown in Figure 15 and Table 5, the splitting tensile strength results at 28 days showed improvement in all GP–GGBFS blended mixtures relative to the control, with CVs of 2.34–6.05%. The GP5S10 mixture recorded the highest tensile strength, reaching 3.9 MPa, an increase of 20% over the control (3.25 MPa), despite its compressive strength remaining nearly unchanged (55.4 MPa vs. 56.0 MPa for CO). This disproportionate gain in tensile strength relative to compressive strength is attributed to an enhancement in the ITZ, where the combined filler effect of GP and the glassy, angular morphology of GGBFS improve paste–aggregate bonding and restrict microcrack propagation under tensile loading [83]. The GP10S20 and GP15S30 mixtures also showed improved tensile strength over the control, reaching 3.6 MPa (+10.8%) and 3.7 MPa (+13.8%), respectively, although both increases were more modest than that of GP5S10. Notably, this trend contrasts with the 28-day compressive strength results, which decreased slightly with increasing replacement level (Figure 13), suggesting that splitting tensile strength is governed more strongly by interfacial bonding quality than by bulk cement content, and that the GP–GGBFS blend continues to enhance the concrete's resistance to tensile cracking even at higher replacement levels.

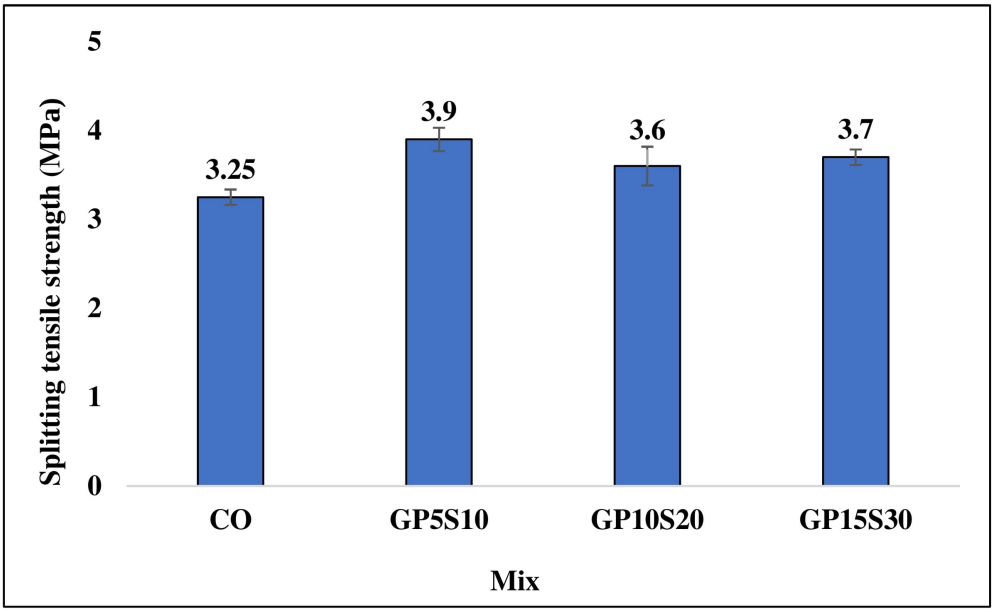


Figure 15. Splitting tensile strength of the SCC mixtures at 28 days.

3.6. Depth of Water Penetration

The depth of water penetration test was conducted to evaluate the resistance of the investigated SCC mixtures to water ingress following the incorporation of GP and GGBFS.

As shown in Figure 16 and Table 5, the CO mixture exhibited a water penetration depth of 18.0 ± 1.7 mm. The standard deviations of the penetration depth ranged from 0 to 1.7 mm (Table 5); the relatively high CV of GP15S30 (14.3%) reflects its small mean depth, at which a difference of 1 mm corresponds to a large relative variation. The incorporation of 5% GP and 10% GGBFS (GP5S10) reduced the penetration depth to 13 mm, representing a 27.8% reduction compared with the control mixture. Further increasing the replacement level to 30% in GP10S20 reduced the penetration depth to 10 mm, corresponding to a 44.4% reduction. The lowest penetration depth of 7 mm was recorded for GP15S30, which incorporated the highest replacement level of 45%, representing a 61.1% reduction relative to the control mixture. The progressive reduction in the depth of water penetration with increasing GP and GGBFS contents indicates improved compactness of the cementitious matrix and enhanced resistance to water ingress. The observed improvement may be attributed to the combined physical and chemical effects of the incorporated materials. The fine particles of GP can fill voids between cementitious particles and improve the packing density of the matrix, while GGBFS can contribute to the formation of additional hydration products that refine the pore structure and reduce the connectivity of capillary pores. These mechanisms can restrict water movement through the hardened concrete and reduce the penetration depth. Overall, the results of this study demonstrate a clear improvement in water penetration resistance as the total replacement level increased from 0% to 45%. The GP15S30 mixture exhibited the lowest penetration depth, indicating the highest resistance to water ingress among the investigated mixtures. The 61.1% reduction in penetration depth relative to the control mixture highlights the potential of combining GP and GGBFS to enhance the durability of SCC against water penetration. However, since both materials were incorporated simultaneously at different replacement levels, their individual contributions to the observed improvement cannot be isolated from the present results.

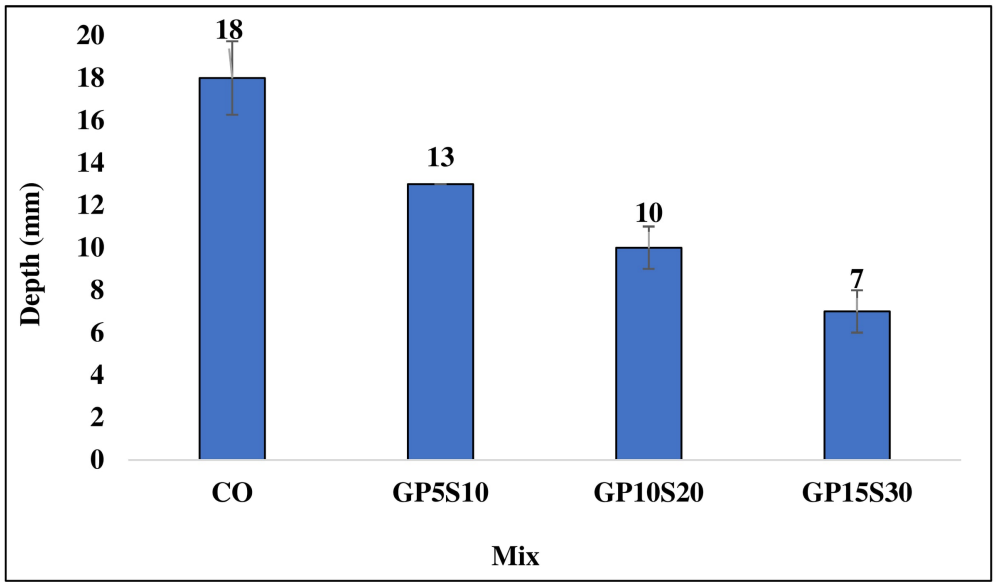


Figure 16. Depth of water penetration of the SCC mixtures at 28 days.

3.7. XRD Analysis

As shown in Figure 17, the XRD patterns of the hardened cement pastes at 28 days reveal the mineralogical changes associated with increasing GP–GGBFS replacement of cement. All four pastes exhibit portlandite (CH) reflections at approximately 18°, 34°, 47° and 51° 2θ, with a feature at about 29–32° 2θ attributed to poorly crystalline C-S-H, which may also include contributions from residual unhydrated clinker phases, and a quartz (Q)

reflection at about 26.7° 2θ. The most diagnostic change across the mix series is the behavior of the portlandite reflections, particularly the peak at approximately 34° 2θ, which remain clearly defined in CO, GP5S10 and GP10S20 but are markedly attenuated in GP15S30. Part of this attenuation reflects the lower cement content of GP15S30 (55% of the binder), which limits the amount of CH that can form during hydration; the remainder is consistent with the consumption of CH by the latent hydraulic and pozzolanic reactions of GGBFS [82] to form additional C-S-H. Because the patterns were not quantified (e.g., by Rietveld refinement or thermogravimetric analysis), these two effects cannot be separated, and the XRD results indicate the direction of the change rather than its magnitude. Conversely, the quartz reflection becomes markedly more intense in GP15S30 than in the other three pastes, where it remains a comparatively minor feature. Because GP itself is predominantly crystalline quartz (Figure 4), this intensification directly reflects the higher GP content at the 45% total replacement level and indicates that GP remained largely unreacted. These mineralogical trends are consistent with the mechanical and durability results: the reduced portlandite content of GP15S30 agrees with its sustained late-age compressive strength gain, its high pozzolanic contribution index ($P = 49.7\%$) at 90 days and its lowest water penetration depth, since the conversion of portlandite to C-S-H refines the pore structure and reduces capillary connectivity. Taken together, the XRD results are consistent with a chemical contribution from the reaction of GGBFS in addition to the physical filler effect of GP.

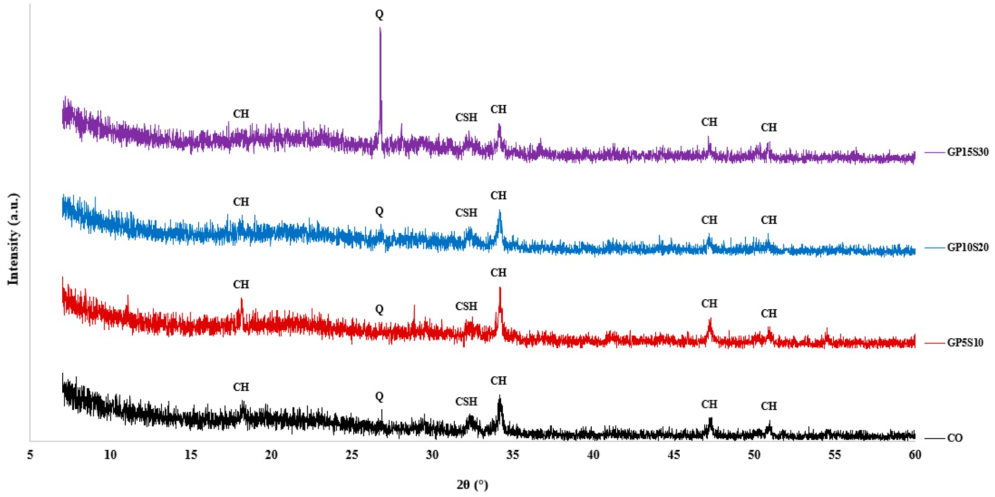


Figure 17. XRD patterns of the hardened pastes at 28 days (CH: portlandite; CSH: calcium silicate hydrate; Q: quartz).

3.8. SEM/EDX Analysis

Figure 18 presents SEM micrographs of the four mixtures at 28 days at two magnifications: ×5000, which shows the overall compactness of the matrix, and ×30,000, which resolves the morphology of the hydration products. Because all images were acquired under identical conditions, the differences between them can be related to the change in binder composition. The micrographs show a clear and progressive transition from a porous, portlandite-rich microstructure in the control mixture to a compact, C-S-H-dominated matrix as the GP–GGBFS replacement level increases, in agreement with the XRD, water penetration, and strength results. The control mixture (CO) exhibited the most heterogeneous and loosely packed microstructure (Figure 18a). Large, stacked, plate-like crystals of portlandite (CH) were abundant, and open pores were visible between the hydrated grains. At higher magnification, well-developed hexagonal CH plates were separated by open voids, into which needle-like ettringite (AFt) crystals projected. The abundance of crystalline CH is consistent with the sharp, dominant portlandite reflection of the CO paste in the XRD

pattern. Because CH contributes little to binding and its large oriented crystals form weak cleavage planes, a CH-rich matrix with interconnected voids provides more pathways for water transport, which is consistent with CO recording the largest water penetration depth (18 mm) among the investigated mixtures.

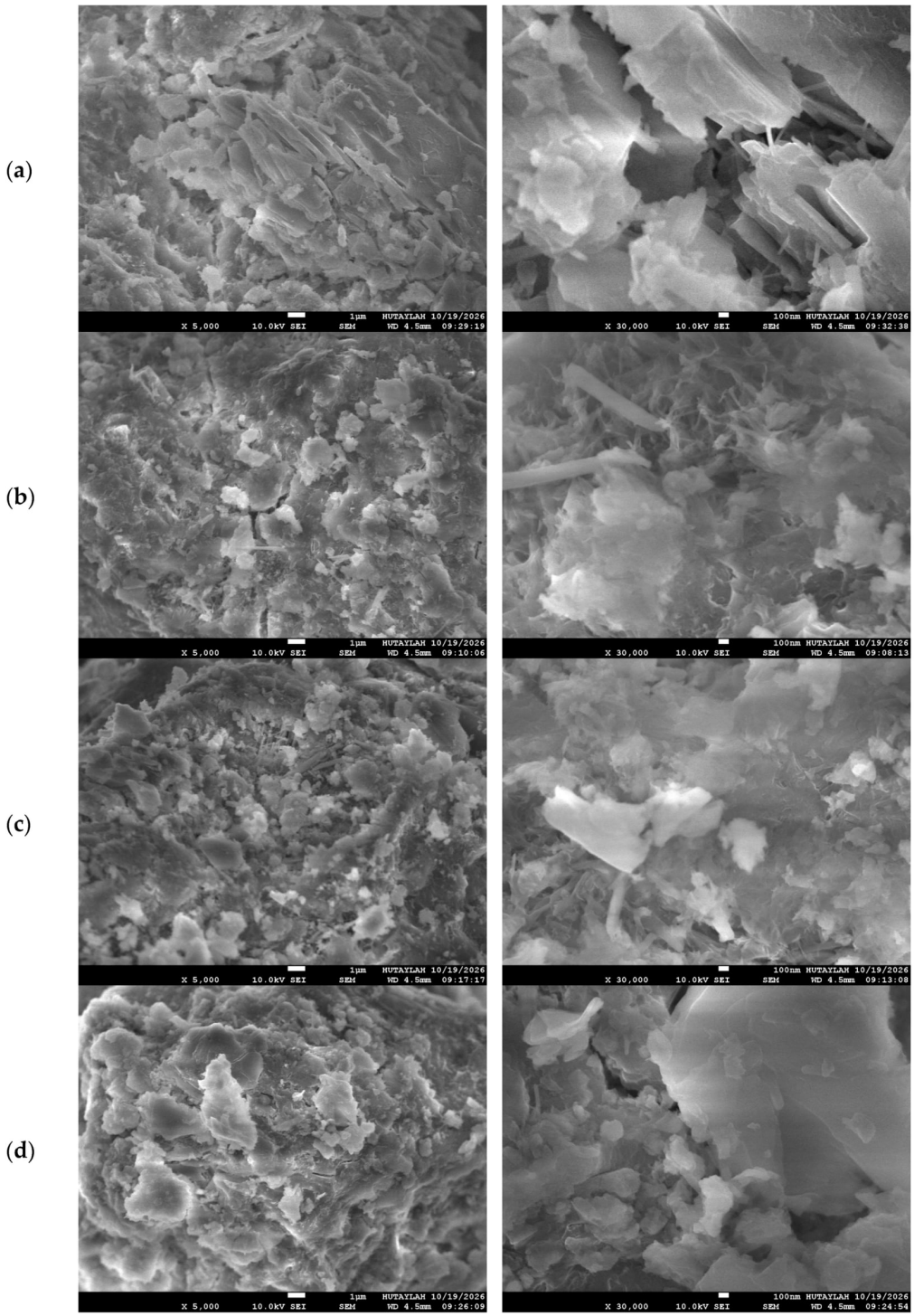


Figure 18. SEM images of the SCC mixtures at 28 days at ×5000 (**left**) and ×30,000 (**right**): (**a**) CO; (**b**) GP5S10; (**c**) GP10S20; (**d**) GP15S30.

With 5% GP and 10% GGBFS (GP5S10), the matrix became noticeably more continuous (Figure 18b). Large stacked CH crystals were no longer prominent, and the surface was dominated by clusters of C-S-H gel. At ×30,000, a fibrous, reticular C-S-H network enveloped

occasional AFt rods and occupied the spaces that appeared as open voids in the control. This refinement agrees with the 27.8% reduction in water penetration depth (13 mm) and with the positive pozzolanic contribution recorded at 28 days ($K = 1.16$, $P = 14.1\%$). A continuous, interlocking C-S-H network is also more effective than a CH-rich matrix at bridging adjacent grains and restricting microcrack propagation, which is consistent with GP5S10 achieving the highest splitting tensile strength (3.9 MPa, +20% relative to CO). At 10% GP and 20% GGBFS (GP10S20), the matrix consisted of fused C-S-H clusters with fine particles packed into the interstices, leaving only small, isolated pores (Figure 18c). The higher-magnification image shows an angular, smooth-faced particle, consistent in morphology with the unreacted GP grains observed in Figure 5, embedded in and bonded to a dense, foil-like C-S-H matrix without a visible gap at its boundary. This image is consistent with distinct roles of the two materials: GP acts as a fine, largely inert filler (D50 $\approx$ 18 μm) that improves particle packing, while the latent hydraulic and pozzolanic reactions of GGBFS supply secondary C-S-H that binds these particles into the matrix. The resulting densification corresponds to the 44.4% reduction in water penetration (10 mm) and the increase in strength efficiency at 28 days ($K = 1.34$, $P = 25.5\%$).

The GP15S30 mixture, with the highest replacement level of 45%, exhibited the densest and most homogeneous microstructure (Figure 18d). The matrix appeared as a continuous, gel-covered mass in which angular grains were firmly embedded, with few open pores visible at this magnification. At ×30,000, a large angular GP grain with smooth fracture faces was surrounded by compact reaction products, and no plate-like CH crystals were observed. These features correspond directly to the XRD results, in which GP15S30 showed the most attenuated portlandite peak and the most intense quartz reflection, reflecting the lower cement content, the consumption of CH by GGBFS and the higher content of crystalline, unreacted GP. The compact microstructure is also consistent with the lowest water penetration depth (7 mm, a 61.1% reduction relative to CO). Although GP15S30 had the lowest early-age strength because of cement dilution, the dense C-S-H matrix already established at 28 days, together with the continued reaction of GGBFS, provides the microstructural basis for its subsequent strength gain to 83.8 MPa at 90 days and the highest pozzolanic contribution recorded in this study ($P = 49.7\%$). Overall, the SEM observations indicate that the improvements in the hardened properties of the GP–GGBFS mixtures arise from the combined physical and chemical effects of the two materials. The progressive replacement of large CH crystals and open voids by a continuous C-S-H matrix, with GP particles acting as embedded fillers, follows the same order as the reduction in water penetration depth (18 → 13 → 10 → 7 mm) and is consistent with the reduction in portlandite identified by XRD.

The EDX results of the 28-day SCC mixtures are summarized in Table 7. In all mixtures, the analyzed matrix consisted mainly of O, Ca and Si, with minor amounts of Al, Fe, Mg, S and K, which is the elemental signature expected for a hydrated cement paste dominated by C-S-H. With increasing GP–GGBFS replacement, the Ca content decreased from 33.67 wt.% in CO to 25.28, 27.49 and 23.06 wt.% in GP5S10, GP10S20 and GP15S30, respectively, whereas the Si content increased to 11.12 wt.% in GP15S30 compared with 8.61 wt.% in CO. Consequently, the matrix Ca/Si mass ratio decreased progressively from 3.91 for CO to 3.05, 3.01 and 2.07 for GP5S10, GP10S20 and GP15S30, respectively, corresponding to a 47% reduction at the highest replacement level. Because each average combines point analyses with partial- and full-field area scans on fractured concrete, the analysed volumes include, in addition to the hydration products, unreacted GGBFS and GP grains and possibly fine limestone or sand particles. The reported ratios therefore describe the overall composition of the matrix rather than the stoichiometry of the C-S-H gel, and the trends between mixtures are more informative than the absolute values.

Table 7. EDX elemental composition (wt.%) of the SCC mixtures at 28 days (average of two point analyses, two partial-area scans and one full-field scan).

Element	CO	GP5S10	GP10S20	GP15S30
C	4.00	9.49	4.62	5.44
O	48.20	48.71	53.04	53.58
Na	–	–	0.06	0.20
Mg	0.94	1.28	1.09	1.56
Al	1.38	2.39	2.10	2.67
Si	8.61	8.28	9.13	11.12
S	0.98	0.74	1.03	0.70
K	0.23	0.46	0.32	0.52
Ca	33.67	25.28	27.49	23.06
Ti	0.05	0.20	0.05	0.15
Fe	1.94	3.18	1.07	1.00
Ca/Si [1]	3.91	3.05	3.01	2.07
Ca/Al [1]	24.40	10.58	13.09	8.64

[1] Matrix mass ratios calculated from the average weight percentages; they describe the analysed matrix volume, which may include unreacted GP and GGBFS grains and fine aggregate particles, and do not represent the stoichiometry of the C-S-H gel. –, not detected.

The high Ca/Si ratio of the control mixture (3.91) reflects the intimate intermixing of C-S-H with portlandite within the EDX interaction volume, in agreement with the abundant plate-like CH crystals observed by SEM and the dominant portlandite reflection of the CO paste in the XRD pattern. The reduction in the matrix Ca/Si ratio to 2.07 in GP15S30 is consistent with a matrix containing less free CH and a lower-Ca, silica-richer composition, in agreement with the consumption of CH by the latent hydraulic and pozzolanic reactions of GGBFS identified by XRD. Part of the reduction in Ca/Si, however, also reflects the chemistry of the binder itself, since replacing cement with silica-rich GP (70.55% SiO_2 and only 1.00% CaO; Table 2) and with GGBFS, which contains less CaO than Portland cement, lowers the Ca/Si ratio of the binder before any hydration occurs, and unreacted GP grains within the analysed volume further contribute Si to the measured composition. The EDX results therefore indicate the formation of a lower-Ca, Si-rich matrix that is consistent with, but does not by itself isolate, the pozzolanic contribution quantified by the strength indices in Table 6.

The Ca/Al ratio is another useful indicator in the EDX analysis of blended binders. A lower Ca/Al ratio reflects a higher alumina content relative to calcium, together with a reduced portlandite content, and favours the formation of Al-bearing hydration products such as C-A-S-H and calcium aluminate hydrates (C-A-H). In the present study, the Ca/Al ratio decreased from 24.40 in CO to 10.58, 13.09 and 8.64 in GP5S10, GP10S20 and GP15S30, respectively (a 65% reduction), as the Al content of the matrix increased from 1.38 wt.% to 2.10–2.67 wt.%. Since both GGBFS (17.86% Al_2O_3) and GP (12.39% Al_2O_3) supply alumina, this is consistent with the uptake of Al into the C-S-H to form an aluminium-substituted C-A-S-H [27], although, as for the Ca/Si ratio, part of this change reflects the Al supplied by unreacted GGBFS and GP grains within the analyzed volume. The lower Ca/Al contents of GP5S10 compared with GP10S20 results from a single Fe- and Al-rich point analysis in GP5S10 (8.02 wt.% Fe and 5.30 wt.% Al), most likely a residual ferrite-rich clinker or Fe-bearing mineral grain, which also explains the higher average Fe content of this mixture (3.18 wt.%). The higher Mg content of GP15S30 (1.56 wt.% vs. 0.94 wt.% in CO) is attributable to the MgO supplied by GGBFS (8.24%), whereas K and Na, the latter detected only in GP10S20 and GP15S30, originate from the alkali feldspar of GP (K_2O = 6.27%, Na_2O = 4.97%), in line with the feldspar reflections identified in GP by XRD and the angular, unreacted GP grains observed in Figure 18c,d. The S content remained low (0.70–1.03 wt.%) in all mixtures, indicating that sulfate-bearing phases such as ettringite were similarly distributed. Carbon (4.00–9.49 wt.%) was detected in all mixtures; because light-element quantification by EDX is

only semi-quantitative and may include contributions from surface carbonation and specimen preparation, C is reported for completeness but was not used in the interpretation. Overall, the EDX results are in agreement with the SEM and XRD observations. The progressive decrease in the Ca/Si ratio (3.91 → 3.05 → 3.01 → 2.07) and the overall decrease in the Ca/Al ratio with increasing GP–GGBFS content are consistent with the attenuation of the portlandite reflections, the transition from a CH-rich to a compact C-(A)-S-H matrix, and the reduction in water penetration depth (18 → 13 → 10 → 7 mm). This supports the interpretation that the improved hardened-state performance of the blended mixtures arises from a combination of GGBFS reactivity and the filler effect of GP.

3.9. Embodied Carbon

As shown in Table 8, incorporating GP and GGBFS as partial cement replacements produced a consistent, progressive reduction in the embodied carbon of the SCC mixtures, with the environmental benefit scaling directly with the level of cement substitution. The control mixture (CO) recorded the highest embodied carbon, 473.3 $kgCO_2e/m^3$, reflecting its reliance on 100% OPC—by far the most carbon-intensive constituent in the mix design (0.82 $kgCO_2e/kg$). As cement was progressively displaced by GP and GGBFS, embodied carbon fell to 424.6 $kgCO_2e/m^3$ (10.3% reduction) for GP5S10, 376.7 $kgCO_2e/m^3$ (20.4% reduction) for GP10S20, and 329.6 $kgCO_2e/m^3$ (30.4% reduction) for GP15S30. This near-linear trend indicates that cement dilution, rather than any secondary effect, is the primary driver of the carbon savings across the mix series. This benefit came at the cost of lower early-age strength, but not of 28-day or later-age performance. GP15S30, in which 45% of the cement was replaced by GP and GGBFS combined, achieved the largest reduction in embodied carbon of all four mixtures while still reaching a 28-day compressive strength of 49.8 MPa (11% below the control) and surpassing the control mixture's strength at 90 days. High-volume replacement of cement by these powders is therefore not simply a trade-off between environmental and structural performance; it represents a genuine efficiency gain, in which less carbon-intensive material is used while strength per unit of cement is preserved, and even enhanced over time, as the continued reaction of GGBFS and the filler effect of GP contribute to strength development beyond 28 days. This efficiency is captured directly by the eco-strength efficiency index, which rose from 0.1183 $MPa{\cdot}m^3/kgCO_2e$ for the control to 0.1511 $MPa{\cdot}m^3/kgCO_2e$ for GP15S30—a 28% improvement. Rather than declining as replacement level increases, the index instead rises steadily across the mix series, showing that each additional increment of cement replaced by GP and GGBFS delivers progressively more compressive strength per unit of embodied carbon invested. Taken together, these results position GP15S30 as the most eco-efficient mixture in the study. It achieves the greatest reduction in environmental impact while preserving, and ultimately exceeding, the structural performance of a conventional 100%-cement SCC mixture—underscoring the practical viability of high-volume GP–GGBFS replacement as a low-carbon design strategy that does not compromise 28-day or later-age strength, provided that its slower early-age strength gain is accommodated.

Table 8. Embodied carbon, reduction relative to the control and eco-strength efficiency of the SCC mixtures.

Mix	CO_2e ($kgCO_2e/m^3$)	Reduction (%)	f_{28} (MPa)	Eco-Strength Efficiency ($MPa{\cdot}m^3/kgCO_2e$)
CO	473.3	0.0	56.0	0.1183
GP5S10	424.6	10.3	55.4	0.1305
GP10S20	376.7	20.4	52.6	0.1396
GP15S30	329.6	30.4	49.8	0.1511

4. Discussion

4.1. Fresh-State Behavior in Relation to Previous Studies

The fresh-state results agree well with previous studies on SCC containing GGBFS and mineral powders. The limited effect of the 15% replacement level on slump flow (737 mm vs. 745 mm for CO) is consistent with reports that low-to-moderate GGBFS contents can preserve or improve the fresh properties of SCC, with workability improvements at replacement levels of up to 20% [60], and with the acceptable fresh properties of self-compacting mortars containing slag and natural pozzolan at replacement levels of up to 35% [84]. GGBFS has also been shown to improve the workability of SCC made with recycled aggregates [85] and to lower the plastic viscosity and yield stress of pumpable concrete [41]. Conversely, the reduction in slump flow at 30% replacement (694 mm) agrees with the observation that excessive powder content increases water demand and viscosity and thereby restricts flow [86], and with reports that granite waste beyond an appropriate level reduces the workability of SCC [87]. The passing-ability results are similarly consistent with the literature: marble and granite powders produced no significant blocking in SCC and, in some cases, improved passing ability with increasing powder content [88]; the passing ability of fiber-reinforced SCC improved at moderate slag contents but deteriorated at higher contents [89]; and J-ring performance remained within acceptable limits despite changes in the blocking ratio with increasing GGBFS content [90]. In the present study, all mixtures remained within a narrow blocking-step range of 2.4–3.5 mm, confirming that the GP–GGBFS blend did not impair passing ability at replacement levels of up to 45%.

Unlike the gradual trends commonly reported for single SCMs, the flowability of the present mixtures was not proportional to the replacement level. Because the superplasticizer dosage was adjusted to maintain self-compactability, the slump-flow and J-ring results reflect the combined effect of binder composition and admixture dosage. The highest flow of GP15S30 (785 mm) is therefore attributable mainly to its higher superplasticizer dosage (1.47% of the binder mass) rather than to an intrinsic effect of the powders, and the effects of powder replacement and admixture dosage cannot be fully separated in the present design. The fine aggregate content differed by at most 4.0% between mixtures, which is too small to account for the observed differences in strength or water penetration, and the influence of the higher superplasticizer dosage on the 28- and 90-day results is expected to be small, because PCE-induced retardation mainly affects the first hours and days of hydration. Tests at a constant superplasticizer dosage supported by rheometric measurements are recommended to separate these effects (Section 4.5).

4.2. Strength Development in Relation to Previous Studies

The strength results indicate a two-stage pattern of strength development. At 7 days, strength was governed mainly by the cement content, and all blended mixtures were weaker than the control, with GP15S30 reaching only 40.5% of the control strength. From 28 days onwards, the latent hydraulic and pozzolanic reaction of GGBFS and the filler effect of GP compensated for the reduced cement content: at 28 days, the blended mixtures were within 1.1–11.1% of the control, and at 90 days GP15S30 reached the highest mean strength of all mixtures (83.8 MPa). This pattern agrees with the behavior reported for high-volume slag and slag–fly ash concretes, in which cement dilution dominates early-age strength [81] while the continued reaction of slag governs the long-term strength gain [82]. It also agrees with the findings of Akhlaq et al. [41], who reported that GGBS reduced the early-age strength of pumpable concrete but produced peak 28- and 56-day strengths at about 40% replacement; this is close to the 30% GGBFS content of GP15S30, which gave the highest 90-day strength and the highest strength efficiency per unit of cement (K = 1.99) in the present study.

These results can be expressed as quantitative regularities. In the dilution-controlled stage (7 days), the strength efficiency per unit of cement remained close to or below that of the control (K = 0.74–1.07), and the 7-day strength decreased by approximately 0.52 MPa per percentage point of replacement (linear fit, $R^2 = 0.92$). In the reaction-controlled stage, K exceeded unity in all blended mixtures at 28 days (1.16–1.62), and the sensitivity of strength to the replacement level fell to approximately 0.14 MPa per percentage point ($R^2 = 0.94$), i.e., by about 73% relative to 7 days; at 90 days, strength no longer decreased with the replacement level. The magnitude of the later-age gain increased with the GGBFS content: the ratio of 90-day to 7-day strength rose from 1.80 for CO to 2.04, 2.17 and 4.84 for GP5S10, GP10S20 and GP15S30, respectively. Across the investigated range, the depth of water penetration (d, mm) and the embodied carbon (CO_2e, $kgCO_2e/m^3$) decreased linearly with the total replacement level (r, %): $d = 17.4 - 0.24r$ ($R^2 = 0.98$) and $CO_2e = 472.9 - 3.19r$ ($R^2 > 0.99$). Because these relationships are based on four mixtures with a fixed GP:GGBFS ratio and a single water-to-binder ratio, they should be regarded as empirical regularities valid within the investigated range.

Regarding GP, moderate contents of about 10% as a cement replacement have been reported as favorable [29], whereas higher contents may reduce strength because of the low reactivity of granite. In the present study, GP contents of up to 15% of the binder did not impair the 90-day strength when combined with GGBFS, which is consistent with studies reporting that inert granite powder can act together with active mineral admixtures [54]. The improvement in splitting tensile strength (up to 20%) despite a slight decrease in 28-day compressive strength is consistent with reports that SCMs improve the ITZ and restrict microcrack propagation [83]. Because GP and GGBFS were added together at a fixed ratio, however, the present results describe the performance of the combined binder rather than the separate contribution of each material.

The slower early strength development of the blended mixtures also has implications for massive SCC elements, in which the heat released by cement hydration can cause high internal temperatures and early-age thermal cracking. Replacing 45% of the cement reduced the clinker content from 514.1 to 282.8 kg/m^3, while GP contributes little heat of reaction and GGBFS releases its heat more slowly than cement. Previous studies have shown that high-volume GGBFS replacement reduced cumulative heat release by up to 36% [51] and the temperature rise of a 1.5 × 1.5 × 2.5 m concrete block by 11.3 °C [52]. High-volume GP–GGBFS SCC may therefore be advantageous for foundations, raft slabs and massive walls, although this should be confirmed by direct thermal measurements, particularly in hot climates, where the heat-reduction benefit of slag is smaller [51].

4.3. Durability and Microstructure in Relation to Previous Studies

The 61.1% reduction in water penetration depth at 45% replacement is consistent with previous studies reporting that GGBFS refines the pore structure, reduces porosity and improves resistance to water penetration [91], and that granite-based fine powders densify the microstructure through their filler effect when used at suitable replacement levels [92]. Lower water penetration depths have similarly been associated with reduced pore connectivity and improved resistance to capillary water transport [93,94]. The present microstructural results provide the corresponding evidence: the attenuation of portlandite in the XRD pattern of GP15S30; the transition from a porous, CH-rich matrix to a compact C-(A)-S-H-dominated matrix in the SEM images; and the decrease in the matrix Ca/Si ratio follow the same order as the reduction in water penetration depth (18 → 13 → 10 → 7 mm).

A lower Ca/Si ratio of C-S-H is generally associated with a more polymerized structure with longer silicate chains [95] and has been linked to improved strength [96,97]. Choudhary et al. [98] found that the concrete with the lowest Ca/Si ratio achieved the

highest compressive strength, and Dadsetan and Bai [99] associated gains in the compressive strength of SCC containing GGBFS with a reduction in the Ca/Si ratio. The present trend, in which GP15S30 had the lowest matrix Ca/Si ratio and the highest mean 90-day strength, agrees qualitatively with these studies. However, because the EDX values describe the overall matrix composition, including unreacted GP and GGBFS grains, and are partly influenced by the change in binder composition and by unreacted GP grains (Section 3.8), this agreement should be regarded as supporting evidence rather than a direct measurement of the gel composition.

4.4. Comparison with Previous Studies

Table 9 summarizes the main results of the present study and compares them with those of similar studies on SCC and concrete containing GGBFS and granite-based powders. Overall, the trends obtained here—maintained self-compactability, an early-age strength penalty followed by later-age recovery, improved tensile strength and resistance to water penetration, and a lower potential for hydration heat—are in agreement with the literature. The main contribution of the present study is that these effects were obtained simultaneously in SCC with a combined GP–GGBFS binder at up to 45% cement replacement, together with a 30.4% reduction in embodied carbon; these aspects were not evaluated together in the studies listed in Table 9.

Table 9. Comparison of the main results of the present study with those of similar studies.

Study	Concrete Type	Replacement Material	Main Findings	Comparison with the Present Study
Present study	SCC	GP + GGBFS (1:2), 15–45% of binder	Slump flow, 694–785 mm; 28-day strength, 49.8–55.4 MPa (control 56.0 MPa); 90-day strength, 83.8 MPa at 45%; tensile strength, +10.8 to +20%; water penetration, −27.8 to −61.1%; embodied carbon, −30.4%	–
Boukendakdji et al. [60]	SCC	GGBFS	Workability improved at replacement levels of up to 20%	Consistent: limited change in slump flow at 15% replacement
Sadek et al. [88]	SCC	Marble and granite powders	No significant blocking; passing ability maintained or improved	Consistent: blocking step 2.4–3.5 mm
Zhao et al. [89]	Fiber-reinforced SCC	GGBFS	Passing ability improved at moderate and deteriorated at high slag contents	Partly consistent: no deterioration up to 30% GGBFS
Jain et al. [23]; Rahmani et al. [29]	SCC and concrete	Granite waste	Favorable at about 10% cement replacement	GP up to 15% of binder without loss of 90-day strength when combined with GGBFS
Akhlaq et al. [41]	Pumpable concrete	GGBS	Lower early-age strength; peak 28- and 56-day strength at 40% replacement	Consistent: early-age penalty and highest later-age strength at 30% GGBFS

Table 9. *Cont.*

Study	Concrete Type	Replacement Material	Main Findings	Comparison with the Present Study
Xu et al. [81]; Liu et al. [82]	High-volume slag concrete	Slag (and fly ash)	Early-age strength reduced by dilution; long-term strength gain from continued slag reaction	Consistent with the two-stage strength development
Yalçınkaya and Çopuroğlu [51]; Woo et al. [52]	UHPC; mass concrete	GGBFS (60% and high volume)	Cumulative heat release of −36% at 20 °C; temperature rise of mass concrete, −11.3 °C	Similar benefit expected from 45% lower clinker content (not measured)
Dadsetan and Bai [99]	SCC	Metakaolin, GGBFS, fly ash	Strength gain associated with a lower Ca/Si ratio	Consistent trend in matrix Ca/Si ratio

From a practical standpoint, the approach is not specific to Saudi Arabia. Granite cutting and polishing generate similar fine slurry residues wherever dimension stone is processed, and the stone industry generates millions of tons of fine waste annually [25], while GGBFS is available in steel-producing regions worldwide [31,32]. The method can therefore be transferred to other regions with granite-processing industries and access to GGBFS, provided that the local GP is characterized for its fineness, mineralogy and alkali content, and that the embodied carbon factor of GP is recalculated using the local electricity grid intensity and the actual drying and grinding energy.

4.5. Limitations

This study evaluated the GP–GGBFS blend as a combined binder system at a fixed GP:GGBFS mass ratio of 1:2, so the individual roles of the two materials were inferred indirectly: the largely inert, filler role of GP from its crystalline mineralogy (Figure 4), the increase in the intensity of the quartz reflection with GP content (Figure 17) and the angular, unreacted GP grains observed by SEM (Figure 18); the reactive role of GGBFS from the strength efficiency values (K) above unity at 28 and 90 days, which cannot be explained by cement dilution alone, and the attenuation of the portlandite reflections. These observations are consistent with complementary physical and chemical roles, but they do not quantify the separate contribution of each material or demonstrate a synergistic interaction, which would require GP-only and GGBFS-only reference mixtures and different GP:GGBFS ratios. In addition, the superplasticizer dosage was varied to maintain equal workability and the fine aggregate content was adjusted to maintain a yield of approximately 1 m^3 (Sections 2.5 and 4.1), so the effects of admixture dosage and powder replacement cannot be fully separated; the microstructural results were also obtained at a single age (28 days). Strength was also measured under a single curing regime; the strength development of SCC containing SCMs, including GGBFS, depends on the curing temperature, for which maturity-based models with a temperature-dependent activation energy have been proposed [100,101]. The GP:GGBFS proportions were not optimized, which could be addressed using machine-learning models for predicting SCC properties [102] and mixture-optimization frameworks that combine machine learning with embodied-carbon assessment [103]. These limitations define the scope of the conclusions below and the directions for future work.

5. Conclusions

This study examined waste granite powder (GP) and ground granulated blast furnace slag (GGBFS), combined at a fixed mass ratio of 1:2, as a replacement for 15%, 30% and 45% of the cement in self-compacting concrete (SCC). The total binder content and the

water-to-binder ratio were kept constant. The fresh, mechanical, durability, microstructural and embodied-carbon performance of the mixtures were assessed together. The three main conclusions are as follows:

1. **Scientific and theoretical result**

- Strength formation in SCC with high-volume GP–GGBFS replacement follows a two-stage pattern: an early, dilution-controlled stage followed by a later, reaction-controlled stage.
- In the early stage, strength is governed mainly by the cement content. The 7-day strength of GP15S30 reached only 17.3 MPa, compared with 42.7 MPa for the control.
- In the later stage, the latent hydraulic reaction of GGBFS and the filler effect of GP compensate for the reduced cement content. The blended mixtures were within 1.1–11.1% of the control (56.0 MPa) at 28 days, and GP15S30 reached 83.8 MPa at 90 days, 9.3% above the control.
- The strength efficiency per unit of cement increased with both age and replacement level, reaching K = 1.99 and P = 49.7% for GP15S30 at 90 days.
- The matrix changed from a porous, portlandite-rich structure to a compact C-(A)-S-H-dominated structure with embedded GP particles. The portlandite reflections were markedly weaker, and the matrix Ca/Si and Ca/Al ratios decreased from 3.91 to 2.07 and from 24.40 to 8.64, respectively.
- Water penetration depth and embodied carbon both decreased almost linearly with the replacement level, by up to 61.1% and 30.4%, respectively.

2. **Engineering, practical and technological result**

- All mixtures met the filling and passing ability requirements of SCC, with slump flows of 694–785 mm (classes SF2–SF3) and J-ring blocking steps of 2.4–3.5 mm. Their flow behavior was governed by the interaction between powder content and superplasticizer dosage.
- All blended mixtures exceeded the control in splitting tensile strength (by 10.8–20%) and in resistance to water penetration.
- The eco-strength efficiency increased from 0.1183 to 0.1511 MPa·m^3/$kgCO_2e$ (+28%), so the blended mixtures deliver more strength per unit of embodied carbon.
- GP5S10 is recommended where early-age and tensile performance are critical. It matched the control at 28 days (55.4 MPa) and gave the highest tensile strength (3.9 MPa).
- GP15S30 is the most eco-efficient mixture, combining the lowest embodied carbon (329.6 $kgCO_2e/m^3$), the highest resistance to water penetration and the highest 90-day strength. It suits structural and precast elements in which slower early strength development can be accommodated through adjusted formwork stripping times and curing.
- The approach can be transferred to other regions with granite-processing industries and access to GGBFS, provided that the local GP is characterized.

3. **Further plans and prospects**

Because GP and GGBFS were incorporated simultaneously at a fixed ratio, their individual contributions could not be isolated. Future research should include GP-only and GGBFS-only reference mixtures and different GP:GGBFS ratios, tested at a constant superplasticizer dosage. Portlandite consumption and hydration products should be quantified by thermogravimetric and quantitative phase analysis, and the composition of the hydration gel should be determined by targeted EDX point analyses of the hydration products away from GP and aggregate particles, complemented by ^{29}Si NMR spectroscopy. Viscosity and segregation resistance should also be measured, and the heat of hydration and temperature rise should be determined by isothermal calorimetry and adiabatic tests to assess suitability for mass concrete. Further work should evaluate long-term durability under chloride, sulfate and carbonation exposure, and extend the embodied-carbon analysis to a full life-cycle and cost assessment.

Author Contributions: Conceptualization, A.A. (Abdullah Alshahrani), A.A. (Abdulaziz Aldawish), H.A.H., T.A.A., M.A.H. and A.A. (Abdulrahman Almajadiah); methodology, H.A.H., T.A.A., M.A.H. and A.A. (Abdulrahman Almajadiah); software, A.A. (Abdulaziz Aldawish); validation, A.A. (Abdulaziz Aldawish), M.A.S. and A.A. (Abdulrahman Almajadiah); formal analysis, A.A. (Abdulaziz Aldawish), H.A.H. and M.A.S.; investigation, A.A. (Abdulaziz Aldawish), H.A.H., T.A.A., M.A.H., M.A.S. and A.A. (Abdulrahman Almajadiah); data curation, A.A. (Abdulaziz Aldawish), A.A. (Ayman Almutlaqah), M.A.S. and A.A. (Abdulrahman Almajadiah); writing—original draft preparation, A.A. (Abdulaziz Aldawish) and H.A.H.; writing—review and editing, A.A. (Abdullah Alshahrani), A.A. (Ayman Almutlaqah), M.A.S. and A.A. (Abdulrahman Almajadiah); visualization, A.A. (Abdulaziz Aldawish) and M.A.S.; supervision, A.A. (Abdullah Alshahrani). All authors have read and agreed to the published version of the manuscript.

Funding: This research was funded by the Deanship of Graduate Studies and Scientific Research at Najran University under the Consortium Funding Program, grant number NU/CPI/SERC/14/3834-4.

Data Availability Statement: The original contributions presented in this study are included in the article. Further inquiries can be directed to the corresponding author.

Acknowledgments: The authors are thankful to the Deanship of Graduate Studies and Scientific Research at Najran University for funding this work under the Consortium Funding Program (grant code NU/CPI/SERC/14/3834-4). The authors also gratefully acknowledge Al Rashed Cement Company, Saudi Arabia, for supplying the ground granulated blast furnace slag used in this study.

Conflicts of Interest: The authors declare no conflicts of interest.

Abbreviations

The following abbreviations are used in this manuscript:

CH	Calcium hydroxide (portlandite)
C-S-H	Calcium silicate hydrate
C-A-S-H	Calcium aluminosilicate hydrate
EDX	Energy-dispersive X-ray spectroscopy
GGBFS	Ground granulated blast furnace slag
GP	Granite powder
ITZ	Interfacial transition zone
LCA	Life cycle assessment
OPC	Ordinary Portland cement
PCE	Polycarboxylate ether
SCC	Self-compacting concrete
SCM	Supplementary cementitious material
SEM	Scanning electron microscopy
SP	Superplasticizer
XRD	X-ray diffraction
XRF	X-ray fluorescence

References

1. Habert, G.; Miller, S.A.; John, V.M.; Provis, J.L.; Favier, A.; Horvath, A.; Scrivener, K.L. Environmental impacts and decarbonization strategies in the cement and concrete industries. *Nat. Rev. Earth Environ.* **2020**, *1*, 559–573. [CrossRef]
2. Marey, H.; Kozma, G.; Szabó, G. Effects of using green concrete materials on the CO_2 emissions of the residential building sector in Egypt. *Sustainability* **2022**, *14*, 3592. [CrossRef]
3. Dahanni, H.; Ventura, A.; Le Guen, L.; Dauvergne, M.; Orcesi, A.; Cremona, C. Life cycle assessment of cement: Are existing data and models relevant to assess the cement industry's climate change mitigation strategies? A literature review. *Constr. Build. Mater.* **2024**, *411*, 134415. [CrossRef]
4. Bukhari, S.J.S.; Moradllo, M.K. Multicriteria performance assessment of 'low w/c + low cement + high dosage admixture' concrete: Environmental, economic, durability, and mechanical performance considerations. *J. Clean. Prod.* **2025**, *523*, 146419. [CrossRef]
5. Barbhuiya, S.; Das, B.B.; Adak, D. A comprehensive review on integrating sustainable practices and circular economy principles in concrete industry. *J. Environ. Manag.* **2024**, *370*, 122702. [CrossRef]

6. Alassaad, F.; Affan, H.; Haddad, B.; Mohamad, A.; Sebaibi, N. Incorporation of concrete polishing waste as a partial substitute for cement in mortar. *Materials* **2025**, *18*, 530. [CrossRef]
7. Qureshi, M.K.; Khan, H.; Shah, M.U.; Bin Zahid, Z.; Rehman, S.U.; Riaz, R.D.; Usman, M.; Ahmad, J.; Kim, I.-H. Sustainable self-compacting concrete incorporating industrial waste SCMs: A state-of-the-art review on rheology, durability, microstructural and mechanical performance. *Innov. Infrastruct. Solut.* **2026**, *11*, 13. [CrossRef]
8. Ghomian, M.; Dehestani, M.; Garshasbi, S.; Azimi, N. Optimizing fracture resistance in steel fiber-reinforced self-consolidating concrete: Insights from mode II and mode I fracture energy analysis. *Structures* **2025**, *75*, 108707. [CrossRef]
9. Zhang, J.; An, X.; Li, P. Research on a mix design method of self-compacting concrete based on a paste rheological threshold theory and a powder equivalence model. *Constr. Build. Mater.* **2020**, *233*, 117292. [CrossRef]
10. Tufail, R.F.; Naeem, M.H.; Ahmad, J.; Waheed, H.; Majdi, A.; Farooq, D.; Maqsoom, A.; Butt, F. Evaluation of the fresh and mechanical properties of nano-engineered self compacting concrete containing graphite nano/micro platelets. *Case Stud. Constr. Mater.* **2022**, *17*, e01165. [CrossRef]
11. Gulec, A.; Kose, M.M.; Gogus, M.T. Experimental investigation of flexural performance of T-section prefabricated cage reinforced beams with self-compacting concrete. *Structures* **2021**, *33*, 2190–2197. [CrossRef]
12. Guo, X.; Liao, L.; Xie, K.; Xu, W.; Lu, L.; Huang, K. Early-age mechanical and shrinkage performance of CaO-MgO expansive agent self-compacting concrete. *J. Build. Eng.* **2025**, *111*, 113165. [CrossRef]
13. Shen, W.; Zhang, Z.; Li, J.; Li, Z.; Wang, Z.; Cao, L.; Rong, G.; Wu, M.; Zhao, D.; Zhao, Z. Experimental investigation on the high-volume fly ash ecological self-compacting concrete. *J. Build. Eng.* **2022**, *60*, 105163. [CrossRef]
14. Long, W.-J.; Gu, Y.; Liao, J.; Xing, F. Sustainable design and ecological evaluation of low binder self-compacting concrete. *J. Clean. Prod.* **2017**, *167*, 317–325. [CrossRef]
15. Aziz, A.; Mehboob, S.S.; Tayyab, A.; Khan, D.; Hayyat, K.; Ali, A.; Latif Qureshi, Q.B.I. Enhancing sustainability in self-compacting concrete by optimizing blended supplementary cementitious materials. *Sci. Rep.* **2024**, *14*, 12326. [CrossRef]
16. Mim, N.J.; Meraz, M.; Islam, H.; Farsangi, E.N.; Mehedi, T.; Arafin, S.A.K.; Shrestha, R.K. Eco-friendly and cost-effective self-compacting concrete using waste banana leaf ash. *J. Build. Eng.* **2023**, *64*, 105581. [CrossRef]
17. Xie, T.; Ali, M.M.; Elchalakani, M.; Visintin, P. Modelling fresh and hardened properties of self-compacting concrete containing supplementary cementitious materials using reactive moduli. *Constr. Build. Mater.* **2021**, *272*, 121954. [CrossRef]
18. Ali, S.T.; El-Dieb, A.; Aboubakr, S.; Taha, M.R. Utilization of ceramic waste powder in self-compacting concrete. In Proceedings of the Fourth International Conference on Sustainable Construction Materials and Technologies (SCMT4), Las Vegas, NV, USA, 7–11 August 2016.
19. Muhammad, A.; Thienel, K.-C. Properties of self-compacting concrete produced with optimized volumes of calcined clay and rice husk ash—Emphasis on rheology, flowability retention and durability. *Materials* **2023**, *16*, 5513. [CrossRef]
20. Adesina, A.; Awoyera, P. Overview of trends in the application of waste materials in self-compacting concrete production. *SN Appl. Sci.* **2019**, *1*, 962. [CrossRef]
21. Wang, X.; Wang, K.; Taylor, P.; Morcous, G. Assessing particle packing based self-consolidating concrete mix design method. *Constr. Build. Mater.* **2014**, *70*, 439–452. [CrossRef]
22. Gautam, L.; Maaze, M.R.; Sharma, K.V. Optimizing self-compacting concrete with bone china ceramic and granite waste for improved mechanical and durability properties. *J. Mater. Civ. Eng.* **2025**, *37*, 04024525. [CrossRef]
23. Jain, A.; Choudhary, S.; Gupta, R.; Chaudhary, S.; Gautam, L. Effect of granite industry waste addition on durability properties of fly ash blended self-compacting concrete. *Constr. Build. Mater.* **2022**, *340*, 127727. [CrossRef]
24. Jain, A.; Maaze, M.R.; Sachdeva, N.; Chaudhary, S.; Gupta, R. Optimizing granite waste aggregate content in self-compacting concrete using multi criteria decision approach. *Sustain. Chem. Pharm.* **2025**, *46*, 102093. [CrossRef]
25. Silva, L.S.; Amario, M.; Stolz, C.M.; Figueiredo, K.V.; Haddad, A.N. A Comprehensive Review of Stone Dust in Concrete: Mechanical Behavior, Durability, and Environmental Performance. *Buildings* **2023**, *13*, 1856. [CrossRef]
26. Zhang, H.; Ji, T.; He, B.; He, L. Performance of ultra-high performance concrete (UHPC) with cement partially replaced by ground granite powder (GGP) under different curing conditions. *Constr. Build. Mater.* **2019**, *213*, 469–482. [CrossRef]
27. Abouelnour, M.A.; El-Aziz, M.A.A.; Osman, K.M.; Fathy, I.N.; Tayeh, B.A.; Elfakharany, M.E. Recycling of marble and granite waste in concrete by incorporating nano alumina. *Constr. Build. Mater.* **2024**, *411*, 134456. [CrossRef]
28. Gehlot, M.R.; Shrivastava, S. An AHP based sustainability assessment of cement mortar with synergistic utilization of granite cutting waste. *J. Build. Eng.* **2024**, *86*, 108794. [CrossRef]
29. Rahmani, F.; Kaci, S.; Ouali, M.O. On the use of self-compacting concrete based on desert sand and granite powder. *Cem.-Wapno-Beton Cem. Lime Concr.* **2024**, *29*, 171–187. [CrossRef]
30. Jain, A.; Gupta, R.; Chaudhary, S. Sustainable development of self-compacting concrete by using granite waste and fly ash. *Constr. Build. Mater.* **2020**, *262*, 120516. [CrossRef]
31. Özbay, E.; Erdemir, M.; Durmuş, H.İ. Utilization and efficiency of ground granulated blast furnace slag on concrete properties—A review. *Constr. Build. Mater.* **2016**, *105*, 423–434. [CrossRef]

32. Benjeddou, O.; Aldahdooh, M.A. Ground granulated blast furnace slag as a supplementary cementitious material in concrete: A comprehensive review. *ES Mater. Manuf.* **2026**, *32*, 2175. [CrossRef]
33. Liu, J.; Wu, Y.; Qu, F.; Zhao, H.; Su, Y. Assessment of CO_2 capture in FA/GGBS-blended cement systems: From cement paste to commercial products. *Buildings* **2024**, *14*, 154. [CrossRef]
34. Kayali, O.; Khan, M.; Ahmed, M.S. The role of hydrotalcite in chloride binding and corrosion protection in concretes with ground granulated blast furnace slag. *Cem. Concr. Compos.* **2012**, *34*, 936–945. [CrossRef]
35. Kim, D.; Kim, C.-Y.; Urgessa, G.; Choi, J.H.; Park, C.; Yeon, J.H. Durability and rheological characteristics of high-volume ground-granulated blast-furnace slag concrete containing $CaCO_3$/anhydrate-based alkali activator. *Constr. Build. Mater.* **2019**, *204*, 10–19. [CrossRef]
36. Hatami, F.; Amiri, M. Experimental study of mechanical properties and durability of green concrete containing slag, waste rubber powder and recycled aggregate with artificial neural network. *Clean. Mater.* **2022**, *5*, 100112. [CrossRef]
37. Li, Q.; Li, Z.; Yuan, G. Effects of elevated temperatures on properties of concrete containing ground granulated blast furnace slag as cementitious material. *Constr. Build. Mater.* **2012**, *35*, 687–692. [CrossRef]
38. Korde, C.; Cruickshank, M.; West, R.P. Hollowcore slab with alternative cementitious materials for winter conditions. *Mag. Concr. Res.* **2021**, *73*, 1060–1070. [CrossRef]
39. Uysal, M.; Yilmaz, K.; Ipek, M. The effect of mineral admixtures on mechanical properties, chloride ion permeability and impermeability of self-compacting concrete. *Constr. Build. Mater.* **2012**, *27*, 263–270. [CrossRef]
40. de Souza, A.M.; de Carvalho, J.M.F.; Santos, C.F.R.; Ferreira, F.A.; Pedroti, L.G.; Peixoto, R.A.F. On the strategies to improve the eco-efficiency of self-compacting concrete using industrial waste: An analytical review. *Constr. Build. Mater.* **2022**, *347*, 128634. [CrossRef]
41. Akhlaq, H.; Peng, T.; Ajmal, M.M.; Khan, M.S.; Riaz, M. Impact of GGBS on the rheology and mechanical behavior of pumpable concrete. *Front. Mater.* **2025**, *12*, 1614951. [CrossRef]
42. Vincent, J.; Natarajan, B.; Das Amaladas, D.; Cruze, D. An Evaluation of Mechanical Properties of Nano GGBFS in Concrete with Statistical Validation. *Buildings* **2023**, *13*, 3060. [CrossRef]
43. Mydin, M.A.O.; Sor, N.H.; Althoey, F.; Özkılıç, Y.O.; Abdullah, M.M.A.B.; Isleem, H.F.; Deifalla, A.F. Performance of lightweight foamed concrete partially replacing cement with industrial and agricultural wastes: Microstructure characteristics, thermal conductivity, and hardened properties. *Ain Shams Eng. J.* **2023**, *14*, 102546. [CrossRef]
44. Razak, R.A.; Hassan, M.A.; Abdullah, M.M.A.B.; Yahya, Z.; Ariffin, M.A.M.; Mansor, A.F.B.; Hao, D.L.C. The Properties of Ground Granulated Blast Furnace Slag Lightweight Aggregate (GLA) at Various Molar Ratio and Its Application in Concrete. *Arch. Metall. Mater.* **2023**, *68*, 991–996. [CrossRef]
45. Nukah, P.D.; Abbey, S.J.; Booth, C.A.; Oti, J. Development of low carbon concrete and prospective of geopolymer concrete using lightweight coarse aggregate and cement replacement materials. *Constr. Build. Mater.* **2024**, *428*, 136295. [CrossRef]
46. Shcherban', E.M.; Stel'makh, S.A.; Mailyan, L.R.; Beskopylny, A.N.; Smolyanichenko, A.S.; Chernil'nik, A.; Elshaeva, D.; Beskopylny, N. Analytical Review of the Current State of Technology, Structure Formation, and Properties of Variatropic Centrifugally Compacted Concrete. *Materials* **2024**, *17*, 1889. [CrossRef]
47. Shcherban', E.M.; Stel'makh, S.A.; Beskopylny, A.N.; Mailyan, L.R.; Meskhi, B.; Elshaeva, D.; Chernil'nik, A. Physical and Mechanical Characteristics of Variotropic Concrete during Cyclic and Continuous Sulfate Attack. *Appl. Sci.* **2023**, *13*, 4386. [CrossRef]
48. Beskopylny, A.N.; Shcherban', E.M.; Stel'makh, S.A.; Mailyan, L.R.; Meskhi, B.; Evtushenko, A.; Varavka, V.; Beskopylny, N. Nano-Modified Vibrocentrifuged Concrete with Granulated Blast Slag: The Relationship between Mechanical Properties and Micro-Structural Analysis. *Materials* **2022**, *15*, 4254. [CrossRef]
49. Bellum, R.R.; Al Khazaleh, M.; Pilla, R.K.; Choudhary, S.; Venkatesh, C. Effect of slag on strength, durability and microstructural characteristics of fly ash-based geopolymer concrete. *J. Build. Pathol. Rehabil.* **2022**, *7*, 25. [CrossRef]
50. Kanaan, D.; Safhi, A.E.M.; Suleiman, A.R.; Soliman, A.M. Fresh, Hardened, and Microstructural Properties of Ambient Cured One-Part Alkali-Activated Self-Consolidating Concrete. *Sustainability* **2023**, *15*, 2451. [CrossRef]
51. Yalçınkaya, Ç.; Çopuroğlu, O. Hydration heat, strength and microstructure characteristics of UHPC containing blast furnace slag. *J. Build. Eng.* **2021**, *34*, 101915. [CrossRef]
52. Woo, H.-M.; Kim, C.-Y.; Yeon, J.H. Heat of hydration and mechanical properties of mass concrete with high-volume GGBFS replacements. *J. Therm. Anal. Calorim.* **2018**, *132*, 599–609. [CrossRef]
53. Leon, G.; Chen, H.-L. Thermal Analysis of Mass Concrete Containing Ground Granulated Blast Furnace Slag. *CivilEng* **2021**, *2*, 254–270. [CrossRef]
54. Lu, L.; Yang, Z.; Li, K.; Zhang, K.; Yan, X.; Marano, G.C.; Briseghella, B. Synergy of inert granite powder and active mineral admixture in manufactured sand mortar: The effect on mechanical properties, chloride permeability and water absorption properties. *Constr. Build. Mater.* **2023**, *408*, 133660. [CrossRef]
55. Crossin, E. The greenhouse gas implications of using ground granulated blast furnace slag as a cement substitute. *J. Clean. Prod.* **2015**, *95*, 101–108. [CrossRef]

56. Li, Y.; Liu, Y.; Gong, X.; Nie, Z.; Cui, S.; Wang, Z.; Chen, W. Environmental impact analysis of blast furnace slag applied to ordinary Portland cement production. *J. Clean. Prod.* **2016**, *120*, 221–230. [CrossRef]
57. Chajec, A. The role of particle size optimisation of waste granite powder in cementitious composites. *Arch. Civ. Mech. Eng.* **2025**, *25*, 274. [CrossRef]
58. Baffoe, E.E.; Bao, S.; Sawadogo, B.; Otoo, S.L.; Huang, M.; Chong, D. The strength of one-part alkaline activated ground granulated blast furnace slag and granite powder binder: Role of sintered red mud incorporation. *Eur. J. Environ. Civ. Eng.* **2025**, *29*, 3498–3526. [CrossRef]
59. Ramakrishnan, K.; Pugazhmani, G.; Sripragadeesh, R.; Muthu, D.; Venkatasubramanian, C. Experimental study on the mechanical and durability properties of concrete with waste glass powder and ground granulated blast furnace slag as supplementary cementitious materials. *Constr. Build. Mater.* **2017**, *156*, 739–749. [CrossRef]
60. Boukendakdji, O.; Kadri, E.-H.; Kenai, S. Effects of granulated blast furnace slag and superplasticizer type on the fresh properties and compressive strength of self-compacting concrete. *Cem. Concr. Compos.* **2012**, *34*, 583–590. [CrossRef]
61. Ravi, G.; Prasanna, P.K.; Satish, S. The Role of Granite Waste Powder on Mechanical and Durability Performance of GGBS and Metakaoline Based Concrete. *IOP Conf. Ser. Earth Environ. Sci.* **2023**, *1130*, 012008. [CrossRef]
62. *ASTM C150/C150M-24*; Standard Specification for Portland Cement. ASTM International: West Conshohocken, PA, USA, 2024.
63. *ASTM C127-25*; Standard Test Method for Relative Density (Specific Gravity) and Absorption of Coarse Aggregate. ASTM International: West Conshohocken, PA, USA, 2025.
64. *ASTM C136/C136M-25*; Standard Test Method for Sieve Analysis of Fine and Coarse Aggregates. ASTM International: West Conshohocken, PA, USA, 2025.
65. *ASTM C128-25*; Standard Test Method for Relative Density (Specific Gravity) and Absorption of Fine Aggregate. ASTM International: West Conshohocken, PA, USA, 2025.
66. BIBM; CEMBUREAU; ERMCO; EFCA; EFNARC. *The European Guidelines for Self-Compacting Concrete: Specification, Production and Use*; SCC European Project Group: Brussels, Belgium, 2005.
67. *ASTM C192/C192M-25*; Standard Practice for Making and Curing Concrete Test Specimens in the Laboratory. ASTM International: West Conshohocken, PA, USA, 2025.
68. *BS EN 12350-8:2019*; Testing Fresh Concrete—Part 8: Self-Compacting Concrete—Slump-Flow Test. British Standards Institution: London, UK, 2019.
69. *BS EN 12350-12:2010*; Testing Fresh Concrete—Part 12: Self-Compacting Concrete—J-Ring Test. British Standards Institution: London, UK, 2010.
70. *BS EN 12390-3:2019*; Testing Hardened Concrete—Part 3: Compressive Strength of Test Specimens. British Standards Institution: London, UK, 2019.
71. *ASTM C496/C496M-17*; Standard Test Method for Splitting Tensile Strength of Cylindrical Concrete Specimens. ASTM International: West Conshohocken, PA, USA, 2017.
72. Yu, L.-H.; Ou, H.; Lee, L.-L. Investigation on pozzolanic effect of perlite powder in concrete. *Cem. Concr. Res.* **2003**, *33*, 73–76. [CrossRef]
73. *BS EN 12390-8:2019*; Testing Hardened Concrete—Part 8: Depth of Penetration of Water under Pressure. British Standards Institution: London, UK, 2019.
74. Collins, F. Inclusion of carbonation during the life cycle of built and recycled concrete: Influence on their carbon footprint. *Int. J. Life Cycle Assess.* **2010**, *15*, 549–556. [CrossRef]
75. Jing, Y.; Lee, J.C.; Moon, W.C.; Ng, J.L.; Yew, M.K.; Jin, Y. Durability and environmental evaluation of rice husk ash sustainable concrete containing carbon nanotubes. *Sci. Rep.* **2025**, *15*, 4352. [CrossRef]
76. Turner, L.K.; Collins, F.G. Carbon dioxide equivalent (CO_2-e) emissions: A comparison between geopolymer and OPC cement concrete. *Constr. Build. Mater.* **2013**, *43*, 125–130. [CrossRef]
77. Thilakarathna, P.S.M.; Seo, S.; Baduge, K.K.; Lee, H.; Mendis, P.; Foliente, G. Embodied carbon analysis and benchmarking emissions of high and ultra-high strength concrete using machine learning algorithms. *J. Clean. Prod.* **2020**, *262*, 121281. [CrossRef]
78. Munro, D.; Di Benedetto, G.; Graham, M.; Jans-Singh, M.; Turpin, M.; Kanavaris, F. The assessment of the embodied carbon of resource-constrained materials including ground granulated blast-furnace slag (GGBS) and ferrous scrap. *Structures* **2025**, *78*, 109175. [CrossRef]
79. *ISO 14044:2006*; Environmental Management—Life Cycle Assessment—Requirements and Guidelines. International Organization for Standardization: Geneva, Switzerland, 2006.
80. Rinchi, B.; Al-Dahidi, S.; Ayadi, O.; Alrbai, M. Techno-economic optimization and life-cycle assessment of off-grid solar co-production of methanol, kerosene, and ammonia from captured CO_2. *Energy Convers. Manag.* **2026**, *366*, 121868. [CrossRef]
81. Xu, G.; Tian, Q.; Miao, J.; Liu, J. Early-age hydration and mechanical properties of high volume slag and fly ash concrete at different curing temperatures. *Constr. Build. Mater.* **2017**, *149*, 367–377. [CrossRef]

82. Liu, S.; Wang, Z.; Li, X. Long-term properties of concrete containing ground granulated blast furnace slag and steel slag. *Mag. Concr. Res.* **2014**, *66*, 1095–1103. [CrossRef]
83. Wu, K.; Shi, H.; Xu, L.; Ye, G.; De Schutter, G. Microstructural characterization of ITZ in blended cement concretes and its relation to transport properties. *Cem. Concr. Res.* **2016**, *79*, 243–256. [CrossRef]
84. Kouider Djelloul, O.; Menadi, B.; Kenai, S. The effect of slag and natural pozzolan on the rheological and compressive strength properties of recycled self-compacting mortar. *Eur. J. Environ. Civ. Eng.* **2024**, *28*, 3793–3810. [CrossRef]
85. Djelloul, O.K.; Menadi, B.; Wardeh, G.; Kenai, S. Performance of self-compacting concrete made with coarse and fine recycled concrete aggregates and ground granulated blast-furnace slag. *Adv. Concr. Constr.* **2018**, *6*, 103.
86. Okamura, H.; Ouchi, M. Self-compacting concrete. *J. Adv. Concr. Technol.* **2003**, *1*, 5–15. [CrossRef]
87. Mohammadsalehi, A.; Mostofinejad, D. Utilization of marble, granite, and travertine sludge as sand replacements in self-compacting concrete with low-carbon binder: Rheological, mechanical, and environmental evaluation. *Constr. Build. Mater.* **2025**, *494*, 143307. [CrossRef]
88. Sadek, D.M.; El-Attar, M.M.; Ali, H.A. Reusing of marble and granite powders in self-compacting concrete for sustainable development. *J. Clean. Prod.* **2016**, *121*, 19–32. [CrossRef]
89. Zhao, Y.; Bi, J.; Sun, Y.; Wang, Z.; Huo, L.; Duan, Y. Synergetic effect of ground granulated blast-furnace slag and hooked-end steel fibers on various properties of steel fiber reinforced self-compacting concrete. *Struct. Concr.* **2022**, *23*, 268–284. [CrossRef]
90. Bheel, N.; Awoyera, P.; Shar, I.A.; Kırgız, M.S. Self-compacting concrete blended with fly ash and ground granulated blast furnace slag. In *Advance Upcycling of By-Products in Binder and Binder-Based Materials*; Elsevier: Amsterdam, The Netherlands, 2024; pp. 309–334.
91. Chen, W.; Wu, M.; Liang, Y. Effect of SF and GGBS on pore structure and transport properties of concrete. *Materials* **2024**, *17*, 1365. [CrossRef]
92. Stempkowska, A.; Gawenda, T.; Chajec, A.; Sadowski, Ł. Effect of granite powder grain size and grinding time of the properties of cementitious composites. *Materials* **2022**, *15*, 8837. [CrossRef]
93. Król, A.; Giergiczny, Z.; Kuterasińska-Warwas, J. Properties of concrete made with low-emission cements CEM II/C-M and CEM VI. *Materials* **2020**, *13*, 2257. [CrossRef]
94. Du, T.; Xiao, J.; Li, C.; Gan, Y.; Jiang, X. Experimental and numerical study on the chloride ions penetration in recycled aggregate concrete. *Constr. Build. Mater.* **2024**, *451*, 138702. [CrossRef]
95. Kim, J.J.; Foley, E.M.; Taha, M.M.R. Nano-mechanical characterization of synthetic calcium–silicate–hydrate (C–S–H) with varying CaO/SiO_2 mixture ratios. *Cem. Concr. Compos.* **2013**, *36*, 65–70. [CrossRef]
96. Elabbasy, A.A.A.; Nabil, I.M.; Mahmoud, K.; Shaaban, S.M.; Abouelnour, M.A.; Mahmoud, A.A.; Mahmoud, A.S.; Fathy, I.N. Effect of nano-magnetite on the engineering and radiation shielding characteristics of high-strength concrete. *Radiat. Phys. Chem.* **2026**, *245*, 113845. [CrossRef]
97. Mahmoud, A.A.; El-Sayed, A.A.; Aboraya, A.M.; Fathy, I.N.; Abouelnour, M.A.; Tayeh, B.A.; Nabil, I.M. Investigating the effects of granite, marble, granodiorite, and ceramic waste powders on the physical, mechanical, and radiation shielding performance of sustainable concrete. *Ann. Nucl. Energy* **2025**, *216*, 111274. [CrossRef]
98. Choudhary, R.; Gupta, R.; Nagar, R.; Jain, A. Mechanical and abrasion resistance performance of silica fume, marble slurry powder, and fly ash amalgamated high strength self-consolidating concrete. *Constr. Build. Mater.* **2021**, *269*, 121282. [CrossRef]
99. Dadsetan, S.; Bai, J. Mechanical and microstructural properties of self-compacting concrete blended with metakaolin, ground granulated blast-furnace slag and fly ash. *Constr. Build. Mater.* **2017**, *146*, 658–667. [CrossRef]
100. Aldawish, A.; Kulasegaram, S.; Almutlaqah, A.; Alshahrani, A. Temperature-adaptive activation energy for maturity-based strength prediction of sustainable, SCM-blended self-compacting concrete. *Materials* **2026**, *19*, 3462. [CrossRef]
101. Aldawish, A.; Kulasegaram, S.; Almutlaqah, A.; Alshahrani, A. From activation energy to equivalent age: An effective machine-learning surrogate for fib-based strength prediction in concretes with supplementary cementitious materials. *Case Stud. Constr. Mater.* **2026**, *25*, e06709. [CrossRef]
102. Aldawish, A.; Kulasegaram, S. Predictive modeling for self-compacting concrete: Evaluating machine learning approaches in real-world construction scenarios. In *Proceedings of the 4th FIB International Conference on Concrete Sustainability (ICCS2024)*; Barros, J.A.O., Cunha, V.M.C.F., Sousa, H.S., Matos, J.C., Sena-Cruz, J.M., Eds.; Lecture Notes in Civil Engineering; Springer: Cham, Switzerland, 2025; Volume 573, pp. 236–242.
103. Aldawish, A.; Kulasegaram, S. Sustainability-focused evaluation of self-compacting concrete: Integrating explainable machine learning and mix design optimization. *Appl. Sci.* **2026**, *16*, 1460. [CrossRef]

Disclaimer/Publisher's Note: The statements, opinions and data contained in all publications are solely those of the individual author(s) and contributor(s) and not of MDPI and/or the editor(s). MDPI and/or the editor(s) disclaim responsibility for any injury to people or property resulting from any ideas, methods, instructions or products referred to in the content.